Elucidation of a Mechanism of Cell Lysis by Chlorhexidine: A Biophysical Approach

Ivana Komljenović, B.Sc.

Brock University, 2008

Department of Physics

Submitted in partial fulfillment
of the requirements for the degree of

Master of Science

Faculty of Mathematics and Sciences, Brock University
St. Catharines, Ontario

Abstract

Chlorhexidine is an effective antiseptic used widely in disinfecting products (hand soap), oral products (mouthwash), and is known to have potential applications in the textile industry. Chlorhexidine has been studied extensively through a biological and biochemical lens, showing evidence that it attacks the semipermeable membrane in bacterial cells. Although extremely lethal to bacterial cells, the present understanding of the exact mode of action of chlorhexidine is incomplete.

A biophysical approach has been taken to investigate the potential location of chlorhexidine in the lipid bilayer. Deuterium nuclear magnetic resonance was used to characterize the molecular arrangement of mixed phospholipid/drug formulations. Powder spectra were analyzed using the de-Pake-ing technique, a method capable of extracting both the orientation distribution and the anisotropy distribution functions simultaneously. The results from samples of protonated phospholipids mixed with deuterium-labelled chlorhexidine are compared to those from samples of deuterated phospholipids and protonated chlorhexidine to determine its location in the lipid bilayer.

A series of neutron scattering experiments were also conducted to study the biophysical interaction of chlorhexidine with a model phospholipid membrane of DMPC, a common saturated lipid found in bacterial cell membranes. The results found the hexamethylene linker to be located at the depth of the glycerol/phosphate region of the lipid bilayer. As drug concentration was increased in samples, a dramatic decrease

in bilayer thickness was observed.

Differential scanning calorimetry experiments have revealed a depression of the DMPC bilayer gel-to-lamellar phase transition temperature with an increasing drug concentration. The enthalpy of the transition remained the same for all drug concentrations, indicating a strictly drug/headgroup interaction, thus supporting the proposed location of chlorhexidine.

In combination, these results lead to the hypothesis that the drug is folded approximately in half on its hexamethylene linker, with the hydrophobic linker at the depth of the glycerol/phosphate region of the lipid bilayer and the hydrophilic chlorophenyl groups located at the lipid headgroup. This arrangement seems to suggest that the drug molecule acts as a wedge to disrupt the bilayer. In vivo, this should make the cell membrane leaky, which is in agreement with a wide range of bacteriological observations.

Contents

Abstract ii

Contents iv

List of Figures vii

List of Tables ix

Acknowledgements x

1 Introduction 1

1.1 Lipids and Membranes 1

1.1.1 Self-Assembly of Lipids 3

1.1.2 Lipid Motions 7

1.2 Liposomal Drug Delivery 9

1.3 Cell Membrane Differences 11

1.4 Chlorhexidine 12

2 ^{2}H NMR in the Study of Lipid Organization 16

2.1 Introduction to Nuclear Magnetic Resonance 17

2.2 Relaxation 20

2.3 Spin-1 Systems 21

2.4 Order Parameter 22

2.5 Distribution Functions and Powder Spectra 24
2.6 De-Pake-ing 26

3 Neutron Diffraction in the Study of Lipid Bilayer Organization . 27
3.1 Introduction to Neutron Diffraction 27
3.2 Reconstruction of the Bilayer 32

4 Differential Scanning Calorimetry in the Study of Lipid Phase Behaviour 35
4.1 Introduction to Differential Scanning Calorimetry 35
4.2 Operation of the Differential Scanning Calorimeter 36
4.2.1 Theoretical Considerations 38

5 The Experiments – Materials and Methods 41
5.1 Deuterium Nuclear Magnetic Resonance 41
5.2 Neutron Diffraction 42
5.3 Differential Scanning Calorimetry 43
5.4 Polarized Light Microscopy 44
5.5 Langmuir Monolayer 44

6 Experimental Results and Discussion 46
6.1 CHX Has a High Affinity for DMPC 46
6.2 Neutron Diffraction Results 48
6.3 Differential Scanning Calorimetry Results 61
6.4 Deuterium NMR Results 67
6.4.1 DePaked Spectra and Orientation of Samples 67

7 Conclusions 77

Bibliography 79

List of Figures

1.1 The fluid mosaic model 2
1.2 Structure of a lipid 4
1.3 Molecular shapes of lipid phases 6
1.4 Motions of phospholipids in membranes 8
1.5 Methods of liposome content release 10
1.6 Chlorhexidine Hydrochloride 13

2.1 Precession of a magnetic moment 18
2.2 Zeeman and quadrupolar splitting 19
2.3 Spin relaxation mechanism 20
2.4 NMR powder patterns 25

3.1 Schematic of neutron diffraction 29

4.1 Schematic of the Shimadzu DSC-60 37
4.2 A typical DSC curve 38

6.1 Polarized light micrographs 47
6.2 Langmuir monolayer result 49
6.3 Raw diffraction data from the neutron diffraction experiments 50
6.4 Rocking curves - neutron diffraction 51
6.5 Water profile of CHX in DMPC 52

6.6 Localization of CHX in a DMPC bilayer by neutron diffraction 54
6.7 CHX configuration possibility - extended, straight-chain 57
6.8 CHX configuration possibility - bent hairpin-like at centre 59
6.9 Effect of CHX-digluconate on DMPC 61
6.10 Endothermic thermograms of DMPC subjected to increasing concentrations of chlorhexidine dihydrochloride 63
6.11 Exothermic thermograms of DMPC subjected to increasing concentrations of chlorhexidine dihydrochloride 64
6.12 Spectra of the pure DMPC sample at various temperatures 68
6.13 DePaked spectra of the pure DMPC sample at various temperatures . 69
6.14 Spectra of the 10:1 DMPC-d_{54}:CHX sample at various temperatures . 70
6.15 DePaked spectra of the 10:1 DMPC-d_{54}:CHX sample at various temperatures 71
6.16 Spectra of the 10:1 DMPC:CHX-d_8 sample at various temperatures . 73
6.17 Depaked spectra of the 10:1 DMPC:CHX-d_8 sample at various temperatures 74
6.18 Matching of motional order 75
6.19 Depaked spectra of the 10:1, 6:1, and 3:1 DMPC:CHX-d_8 samples at 25°C 76

List of Tables

3.1 Bound atom scattering lengths and cross-sections. 34

6.1 Transition temperature, peak width, and enthalpy data recorded from the endothermic DSC scans. 66

6.2 Transition temperature, peak width, and enthalpy data recorded from the exothermic DSC scans. 67

Acknowledgements

I would like to thank my supervisor, Dr. Edward Sternin for his guidance, help, and patience throughout this project. Thank you for giving me the opportunity to work in the lab, for challenging my abilities and knowledge, and for encouraging me to constantly better myself.

I would like to thank the members of the Physics Department at Brock for their support over the course of my undergraduate and graduate studies, for their teachings, and for all the opportunities they have given me.

Thank you to my committee, Dr. Thad Harroun and Dr. Božidar Mitrović for their guidance, and help over the course of my project.

Thank you to the Hudlicky group, for the synthesis of the deuterated chlorhexidine.

Thank you to my lab-mates, Drew, Sedigh, Brad, Michelle and Shawn.

Many thanks to my friends for all your advice, help, friendship and fun times throughout these past few years.

Thank you to my parents, brother and family for your caring, love and support throughout these years. Without you, I would not be who I am today.

Chapter 1

Introduction

1.1 Lipids and Membranes

The central paradigm of the importance of membranes in cell biology is the connection between the function of the cell and the occurrence and structure of fluid biological membranes. The cell is the structural and functional unit of all living organisms. Two classes of cells exist; prokaryotic cells, which lack a nuclear envelope and a nucleus, and eukaryotic cells, which contain a nucleus and other specialized membrane-bound organelles, which in turn are internal compartments where specific metabolic activities take place. Both classes of cells have one component in common, that being the cell membrane. The membrane is the outer casing of any living cell. It separates the interior components from the external chemical environment, allowing the intracellular components to freely move and work in their own micro environment. The cell membrane is relatively permeable to water, but quite impermeable to large molecules and ions, allowing the cell to control its internal chemical environment. Should the cell membrane rupture or break, the leakage of intracellular components induces lysis (death) of the cell.

The main topological function of the membrane is to serve as a divider between the exterior aqueous phase and the cell's internal micro environment. However, many biological and biochemical processes could not occur without the cell membrane. Many of these processes occur with the aid of enzymes and proteins which function

as biochemical catalysts. Many enzymes are either membrane-bound, or at least membrane associated [1].

The membrane itself is made up of a bilayer of lipids. This layer is also known as the fluid mosaic membrane. Singer and Nicolson [2] developed a fluid mosaic model based on thermodynamic conditions and experimental evidence. The mosaic model for membranes is a structure in which globular molecules of integral proteins alternate with large sections of phospholipid bilayer in the cross-section of the membrane. Both the globular proteins and the phospholipids are amphipathic, meaning these compounds contain both a hydrophobic and a hydrophilic region.

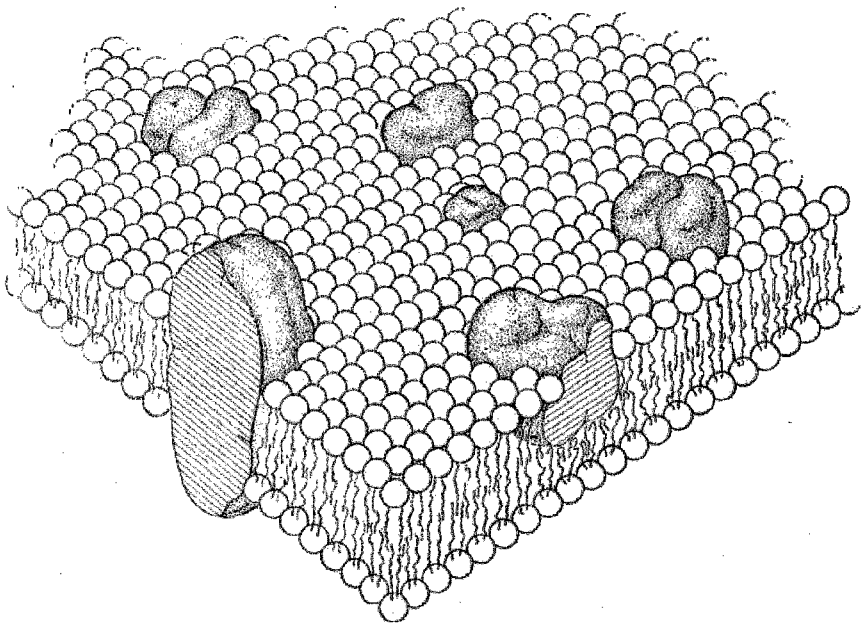

Figure 1.1: The fluid mosaic model, as proposed by Singer and Nicolson [2].

The hydrophilic (polar) region is covered in clusters of ionic amino acids and covalently bound saccharide residues, and it is this region that is in direct contact with the aqueous phase. The hydrophobic (non-polar) region is devoid of such ionic and saccharide residues, and is embedded in the interior of the membrane. The extent

to which the proteins and other such large molecules are embedded in the bilayer, and the extent to which they are in contact with the aqueous phase is determined by thermodynamics. This amount of contact between the proteins and the aqueous phase is determined by the amino acid sequence, the covalent structure of the protein and by the protein's interaction with its molecular environment, so that the free energy of the system is at a minimum. Some integral proteins may even traverse the entire membrane.

The phospholipids of the mosaic structure are predominantly arranged as a bilayer interrupted with these integral proteins, with their polar headgroups in contact with the aqueous phase. The thickness of the mosaic membrane varies along the surface depending on how many proteins are present in any given section. With experimental evidence, Singer and Nicolson [2] proposed the long-range fluid mosaic structure with the lipids constituting the matrix. Using this model, the fluidity (here meainf the viscosity of the lipid bilayer) introduces a factor into the speculation of certain membrane functions. The physical or chemical perturbation of a membrane is able to affect or alter a particular membrane component or set of components. Through translational diffusion (the movement of a lipid or protein with a neighbour), a redistribution of membrane components can occur through the viscous 2D solution, allowing for new thermodynamic interactions among the altered components to take effect. Such a general mechanism has been proposed to play an important role in various membrane-mediated cellular phenomena that occur on a time scale of minutes or longer (ex. mitosis, food transport, *etc.*).

1.1.1 Self-Assembly of Lipids

Lipids are a heterogeneous designation for organic molecules that have little or no affinity for water. This group of molecules includes fats, oils, waxes, steroids, and

phospholipids. Phospholipids are amphipathic, meaning they have both a polar region (the headgroup which is hydrophilic due to an unshared electron pair) and a non-polar region (the hydrophobic hydrocarbon tail). These lipids are classified according to the structure of their hydrocarbon chains; they can be saturated (all carbon-carbon bonds are single bonds), unsaturated (have some double bonds between carbons), or even contain complex side groups.

The most common of cell membrane lipids are the glycerophospholipids, also known as glycerol phosphatides or phosphoglycerides. As illustrated in Figure 1.2, these phospholipids are made up of a glycerol backbone, two fatty-acid chains, and a phosphate group which can be attached to a variety of headgroups.

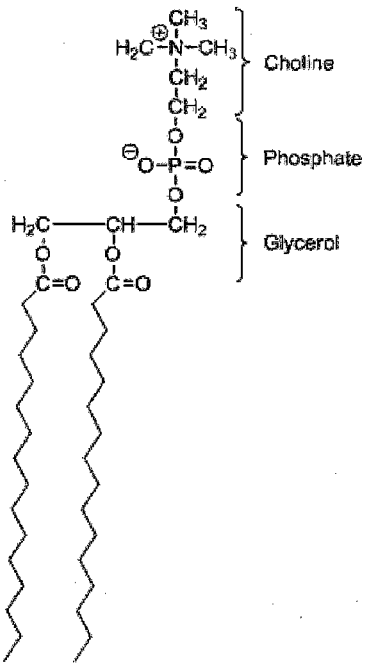

Figure 1.2: Phosphatidylcholine is the most common phospholipid in cell membranes.

When in contact with a polar solvent (*i.e.* water), phospholipids will self-assemble in any number of structural phases, in order to minimize the free energy of interaction with the polar solvent. The structural phase preferences of lipids is determined by a

wide variety of factors including hydrocarbon unsaturation, temperature, headgroup size, headgroup ionization, and water of hydration concentration.

Common structures are lamellar, hexagonal, crystalline, 2D oblique, and cubic. The bilayer is the most common structure of the lipid/water assembly. In this phase, headgroups of two monolayers are pointed opposite one another, and these headgroups are in contact with the aqueous phase, while the fatty acid chains of the monolayers are in contact with one another, due to their hydrophobicity. Phospholipid bilayers account for nearly 50% of most eukaryote cell plasma membranes and there are approximately 5 million lipid molecules in 1 μm^2 of bilayer [3]. Bilayers of lipids can further assemble into liposomes, multi-lamellar vesicles or tubules. A liposome is a vesicle (sack) composed of a bilayer enclosing an aqueous compartment. They are approximately spherical, and can exhibit surface waves and undulations. A multi-lamellar vesicle is onion-like, with multiple bilayers separated by aqueous solution layers. The number of bilayers is typically 50 to 100. A tubule is a hollow microcylinder with one or more bilayers.

For the most part, lipids of the same type follow the same thermotropic behaviour, that is to say, that as the lipid/water systems are heated up, the lipids form different structural phases in a predictable pattern. Lipids tend to follow the general pattern of lamellar-to-hexagonal-to-cubic phases [4]. The onset of a phase is dependant on the shape of the lipid and its concentration.

A simple property to determine the lipid shape is a dimensionless parameter defined as

$$S = \frac{\nu}{a_o l_c}\,, \tag{1.1}$$

where a_o is the optimum area per molecule at the lipid/water interface, ν is the volume per molecule, and l_c is the length of the fully extended acyl chain. Lipids with a shape parameter of S<1 prefer a "cone" shape, S=1 corresponds to a cylin-

drical shape preference, and S>1 corresponds to an "inverted cone" shape preference (see Figure 1.3) [4]. Lysophospholipids have an inverted cone shape, and thus are often found as micelles. Phosphatidylcholines (PC), phosphatidylserines (PS), phosphatidylglycerols (PG), phosphatidic acid (PA), and sphingomyelin all have a cylindrical shape, making lamellar phases the most common to these headgroups. Phosphatidylethanolamine (PE), PA, and PS lipids at low pH (*i.e.* less than pH 4) have cone shapes, making the inverted micelle (also known as the hexagonal phase), their preference [5]. Although each lipid type has its preference, structural phases do not occur spontaneously; surrounding temperature and concentration of lipids must be increased in order to see a phase transition. The preferences mean that the preferred phases occur at a lower transitional temperature than in other lipids. For example, since PE lipids are cone-shaped, the hexagonal phase is observed at a lower temperature in PE lipids than in PC lipids, which are cylindrically shaped, and prefer the lamellar phase.

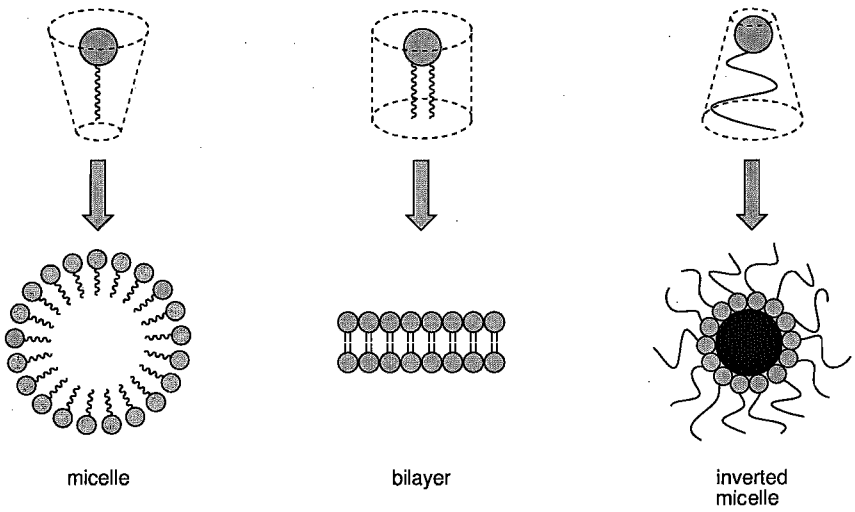

Figure 1.3: The molecular shapes of the three main lipid phases: micellar, lamellar, and hexagonal (also known as inverted micellar).

1.1.2 Lipid Motions

The lipid bilayer is a 2D fluid matrix where the phospholipid molecules are able to move in a number of ways (Figure 1.4). The lipids themselves are able to move within the bilayer to new locations. The basic types of lipid motions include lateral diffusion, transverse diffusion, rotational diffusion and trans-gauche isomerization.

Lateral diffusion of the lipids is the movement of one lipid exchanging places with a neighbour in the same monolayer. Transverse diffusion is the movement of one lipid from one monolayer to the other. This motion is commonly known as "flip-flop". Rotational diffusion is the movement of the lipid about its long axis. Trans-gauche isomerization is the name associated with the intrachain motions of the lipid (ex. flexing, kink formation, *etc.*).

Each motion has a specific timescale. Lateral diffusion occurs on a timescale of 10^7 movements per second. At the slow end of the spectrum is the transverse ("flip-flop") motion. These motions occur on the order of one lipid every few seconds due to the large activation energy barrier. Rotational diffusion about the long axis occurs on the order of 10^9 times per second. The fastest motions are the trans-gauche motions [6, 7]. Motions can be sped up with the help of integral enzymes. This is especially true of the transverse motion; the lipid can flip faster with the help of the enzyme Flippase, which helps the hydrophilic headgroup pass quickly through the hydrophobic tail region [6, 8].

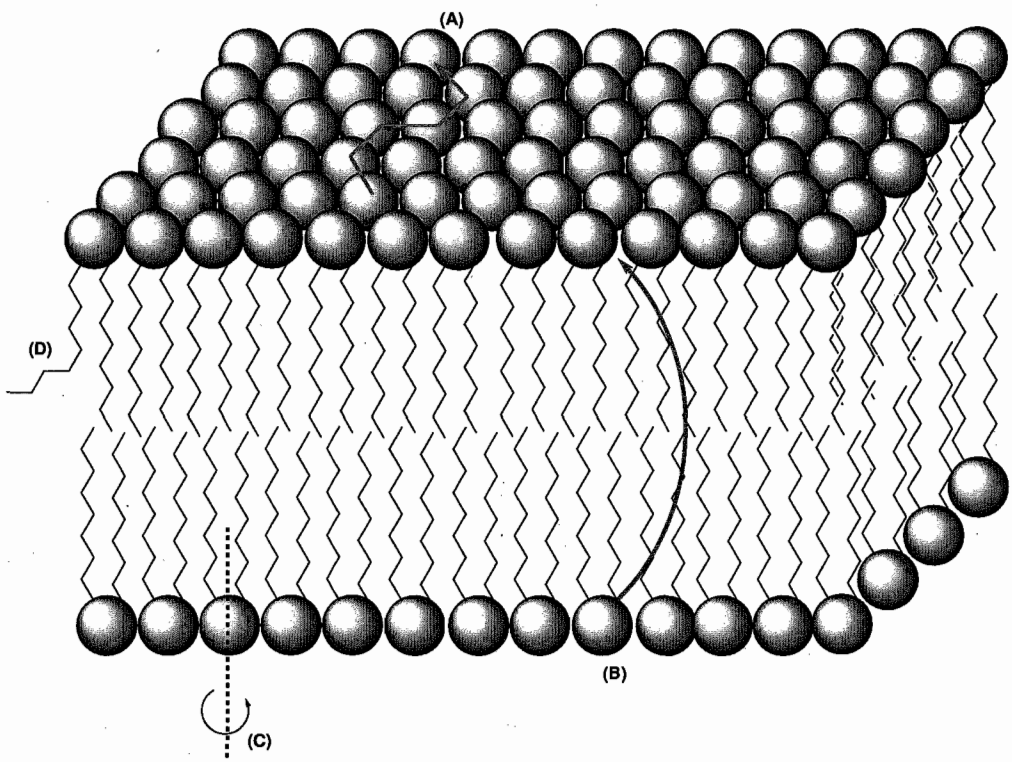

Figure 1.4: Motions of phospholipids in membranes. (a) lateral diffusion; (b) transverse diffusion; (c) rotational diffusion (re-orientation about its long axis); (d) trans-gauche isomerization.

1.2 Liposomal Drug Delivery

Polymorphism of lipid bilayers make them suitable as a drug carrier. The goal is to trap a water-soluble drug inside the lipid bilayer shells, tubules or liposomes. With a careful control of the lipid composition, slow-leaking drug carriers for targeted delivery through an aqueous medium such as blood or saliva can be formed. Site-specific molecules, such as antibodies can be incorporated into the bilayer. These molecules are able to recognize and attach to particular antigens, and so can easily identify the target cell, thus delivering the drug near the attachment sites. This can maximize the therapeutic effect, and minimize any possible toxic effect elsewhere. A drug encapsulated by a liposome is protected from early release, and possible degradation within the body. The fact that the liposome is a "sack" of liquid surrounded by lipid helps reduce dosage and can extend the effect of the drug [9]. The drug's rate of release is dependent on the drug properties, liposome composition, pH of the medium and several other factors.

Liposomes release their contents in one of four ways: adsorption, endocytosis, lipid exchange or fusion [10, 11]. During adsorption, the contents are leaked slowly into the extracellular fluid and then absorbed across the membrane. During endocytosis, the cell engulfs the entire liposome. This process occurs when the contents are polar or too large to pass through the membrane. During lipid exchange, the individual lipid molecules transfer from the liposome to the plasma membrane. Only the drugs associated with the lipids are delivered this way; the entire contents are not transferred to the cell. During fusion, the outer membrane of the liposome is intercalated with the cell membrane, with a release of the aqueous contents directly into the cell cytoplasm. Figure 1.5 illustrates the different methods of liposome content release.

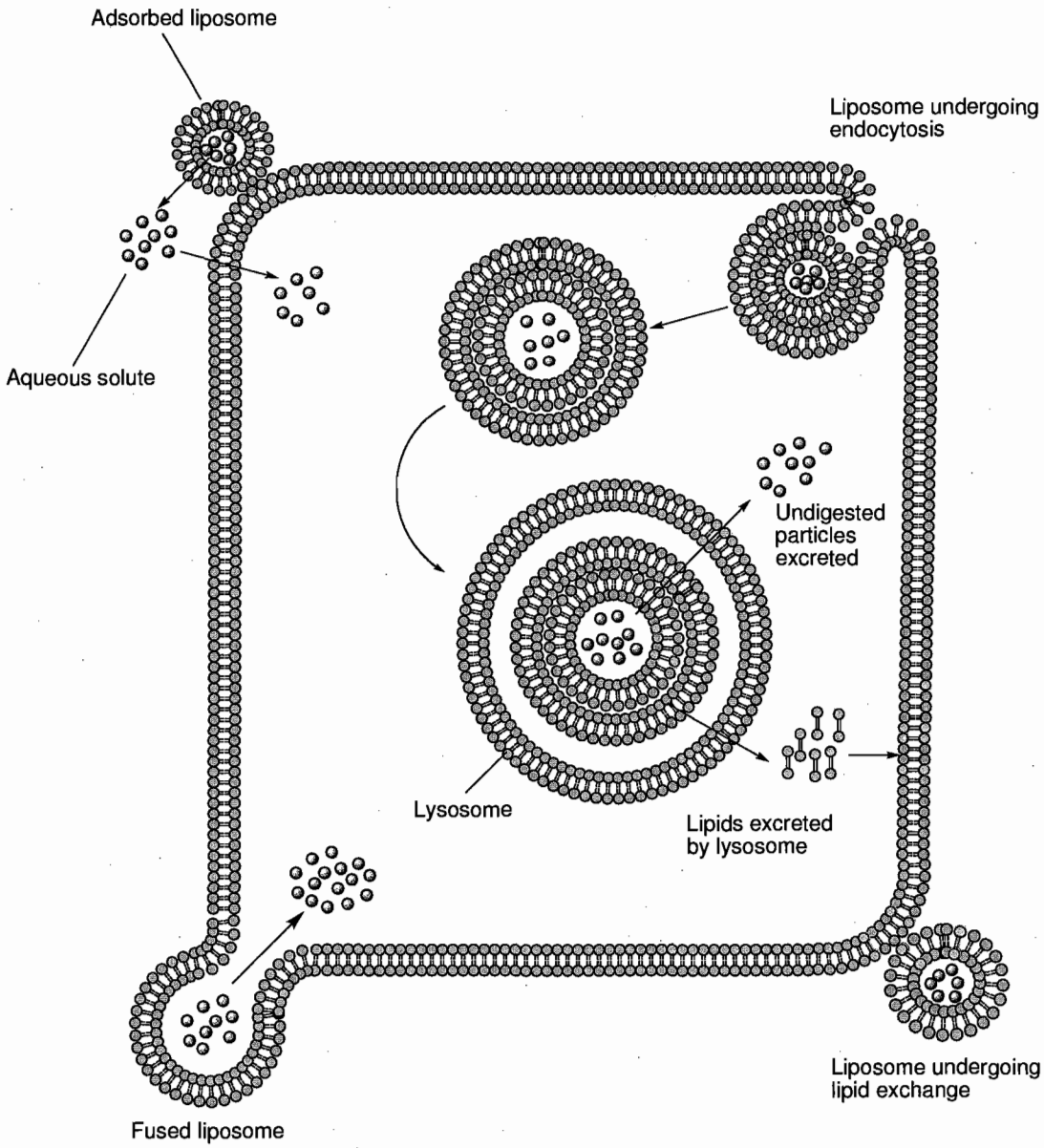

Figure 1.5: The different methods by which liposomes release their contents. Figure reproduced from [10].

1.3 Cell Membrane Differences

The cell structure of prokaryotic and eukaryotic cells differ greatly. The defining characteristic of the prokaryote is the fact that it lacks a nucleus (its genetic material is not membrane-bound), and other membrane-bound organelles. Eukaryotes are highly complex cells with many membrane-bound structures within it.

Bacterial cells are not compartmentalized, and are thus considered to lack organelles. The genetic material consists of a single chromosome, a tightly bundled long strand of DNA that lies within the cytoplasm not surrounded by any nuclear membrane. This means that all bacteria possess a prokaryotic form of organization [12].

Both prokaryotic and eukaryotic cells have a common structure in the cell membrane. The small differences in cell membrane structure allow for the interaction of antibiotics with bacteria, but not human cells.

Eukaryotic cell membranes are typically comprised of phosphoglyceride lipids (<50%), proteins (~50%), and sterols (such as cholesterol, which is required for proper membrane permeability and fluidity in mammalian cells).

All bacteria possess a cell membrane of the typical bilayer structure. The bilayer consists of phospholipids and embedded proteins. In some bacterial cells, up to 70% of the cell membrane is comprised of proteins [13]. This is a considerably higher proportion than found in typical eukaryotic mammalian cells. The cell membrane is the osmotic barrier for the bacterium, and it is protected by one of two types of cell wall. This cell wall provides rigid mechanical support for the bacterium, preventing pressure buildups from bursting the cell. It is also a chemical and physical defence against toxins trying to enter the bacterial cell. There are two main types of bacterial cell wall: gram-negative, and gram-postive, so named for their staining ability.

Gram-positive cell walls consist of a thick multimolecular coat of peptidoglycan, with teichoic acids interspersed. This polymeric fabric consists of many layers wrapped around the cell, thereby forming a sack that determines the shape and size of the bacterium. This multilayered wall impedes the passage of hydrophobic compounds, because the wall is highly polar.

In gram-negative bacteria, the peptidoglycan layer is much thinner than in gram-positive bacteria, and a separate membrane is present outside this peptidoglycan layer. The outer membrane is chemically distinct from the usual biological membranes. It has a bilayer structure, but only the inner monolayer has a composition resembling the cytoplasmic membrane. The outer monolayer has a unique constituent in the place of phospholipids. This component is the lipopolysaccharide. As a result, the bilayer is highly assymetrical [13]. Porin is also dispersed throughout the outer cell membrane. Porin is a transmembrane protein, acting as a channel for the passive diffusion of molecules.

1.4 Chlorhexidine

An effective biocide, chlorhexidine (CHX, Figure 1.6) is a drug used widely in antiseptic products, especially in hand washing and oral products (*e.g.* mouthwash), and has potential applications in the textile industry [14, 15, 16]. It has been used widely in the practice of medicine for the treatment of burns and disinfection of the skin [17]. It is a well-known inactivating agent of many nonsporulating bacteria, it has some sporostatic and mycobacteriostatic action, and it is effective against yeasts and protozoa [18].

Initial investigations of CHX effectiveness as a bactericidal agent were done over 40 years ago by Hugo and Longworth [19], who noted that the uptake of the drug was

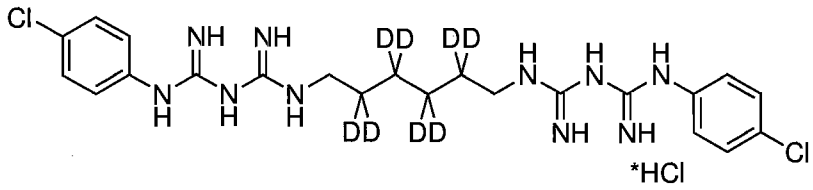

Figure 1.6: Chlorhexidine hydrochloride, deuterium labelled on the hexamethylene.

very quick and was dependent on the concentration of CHX and pH of the system. More recent studies done by Fitzgerald *et al.* [20] using ^{14}C-labelled chlorhexidine gluconate, found that the uptake by bacteria and yeasts occurred within seconds, and a maximal effect of the drug occurred within 20 seconds.

The path of CHX uptake is of great interest, since it can reveal the drug's mode of action. Through hydrophobicity (hydrocarbon response) and antibacterial sensitivity tests, El-Moug *et al.* [21] discovered that the drug initially causes considerable damage to the outer cell layers of bacteria or yeast. However, this damage was not found to be a major cause of cell death, since the drug continues on to attack the cytoplasmic membrane of bacteria, or the plasma membrane in yeast. Hiom *et al.* [22] studied changes in viability, changes in optical density, and looked at the leakage of intracellular components through spectrophotometry, and found that CHX partitions into the plasma membrane and cytoplasm of cells. Though the mechanism of this trans-membrane transport is not clearly understood, it is followed by a leaking of intracellular components as a consequence of semipermeable membrane damage. At high concentrations of CHX, there is a coagulation of the intracellular components, followed by a reduction of leakage [19]. Although leakage of the intracellular components increases with an increase in CHX concentration initially, beyond a certain critical point, the leakage is reduced as a result of this coagulation. Barrett-Bee *et al.* [23] called this a "gelling" effect of the drug. This should not be confused with

the gel state of the lipids.

Although early research of the mode of action of CHX described an inactivation of ATPase, more recent studies have concluded that it is the membrane disruption by CHX that is associated with its lethal effects. ATP concentrations are reduced by CHX, but it is a very slow process. It is now thought that the lethal effects are a result of the membrane disruption that occurs within seconds [23, 24, 25].

Biological observations show that CHX has little to no-effect on a number of bacterial spores, nor is it effective against many bacteriophages, and its antiviral action is limited to lipid-enveloped viruses (*i.e.*, a membrane must be present) [18, 26]. There have been studies on the effect of sub-lethal doses of CHX on metabolic processes on biofilms encountered in clinical and natural settings. CHX creates morphological changes and tightly associates with the lipid effluent from treated *Pseudomonas fluorescens*, and not the protein or lipopolysaccharide components [27, 28, 29]. The dose dependence of CHX against natural biofilms is indicated by damage to the plasma membrane. In sub-lethal concentrations, incorporation of CHX drastically alters the lipid composition of *Candida albicans* [30, 31, 32]. This has a profound effect on membrane fluidity, indicative of CHX's lipophilic properties. Tests done on *E. coli* demonstrate a marked effect on the inner membrane, with some evidence of lipid phase separation and domain formation of the acidic phospholipids in the cytoplasmic membrane through fluorescence polarization measurements [33]. Effects of CHX on yeasts is thought to be similar to those on bacteria. Studies of yeast cells by Hiom *et al.* [22] found that with an increase in CHX concentration, there is an increase in protoplast lysis, until the concentration of the drug exceeds 25 μg/mL, which is marked by a reduction in lysis.

Structurally, chlorhexidine belongs to the family of N^1, N^5-substituted biguanides. It is found in a bis configuration, with a hexamethylene connector, and chlorophenol

rings at the ends. The hexamethylene connector at the centre confers a hydrophobic component, and the cationic nature of the biguanide adds a hydrophilic and ionic component. In literature, each characteristic has been separately stated as the mode of action against membranes, as noted in the tests where bisbiguanides with different N^5 derivatives had their bactericidal efficacy tested [34, 35]. In the case of chlorhexidine, it is more likely that both components of the drug play important roles. The aromatic rings are lipophilic, and in recent literature, aromatic rings have been accepted as lipid/water anchoring motifs, especially in proteins [36, 37, 38].

The molecular structure of chlorhexidine in various environments has not been highly investigated, and thus there is no reason to exclude most molecular configurations. The hexamethylene linker at its centre has a potential to bend in various ways, allowing the stacking of the chlorophenol rings through π-interactions. The linker could also remain rigid, extending chlorhexidine to its full length. An extended chlorhexidine molecule that lies across the lipid bilayer is an appealing configuration for lysis, since the hexamethylene would be fully buried within the hydrophobic environment of the lipid tails. However, the length of the fully extended CHX is not long enough to raise all of the amines above the hydrophobic region [39]. This would be energetically unfavourable. The following biophysical experiments were conducted to provide insight into the molecular basis of chlorhexidine's mode of action.

Chapter 2

^{2}H NMR in the Study of Lipid Organization

The accurate determination of the molecular structure of biological molecules is imperative in understanding their function. Nuclear magnetic resonance (NMR) is a versatile technique used in determining molecular structure. In the spectra of solutions, anisotropic interactions are averaged to zero by fast and isotropic motion, while in solids, the distribution of orientations is only partially averaged, leading to the ovelap of spectral lines, and the inability to resolve some specific residues within the solid.

Lipid membranes are not real solids. In a fluid membrane, lipids undergo fast rotational motions about the bilayer normal. Segments of lipids can also undergo fast motion in limited angular domains. Due to this, average orientations can be determined and order parameters thus express the amplitudes of these local motions [40]. ^{2}H NMR is sensitive to the local orientations of the C-D bond in a lipid tail because the nuclear quadrupolar moment interacts with the electric field gradients surrounding the C-D bond. It is in this way that ^{2}H NMR of lipid membrane samples is useful in providing a picture of the local molecular motions, leading to hypotheses of molecular structure.

2.1 Introduction to Nuclear Magnetic Resonance

The magnetic moment $\vec{\mu}$ of a nucleus is proportional to the intrinsic spin angular momentum $\vec{S}$ through

$$\vec{\mu} = \gamma \vec{S} \,, \tag{2.1}$$

where γ is the gyromagnetic ratio, a scalar property specific to every nucleus. When the nuclei are exposed to an external magnetic field $\vec{H}_0$, their magnetic moments interact with the field, and yield a net magnetization:

$$\vec{M} = \sum_i \vec{\mu}_i \,, \tag{2.2}$$

and this net magnetization is governed by

$$\frac{\mathrm{d}\vec{M}}{\mathrm{d}t} = \gamma \vec{M} \times \vec{H}_0 \,. \tag{2.3}$$

The solution to this equation is the classical precession of the net magnetization about a field, at a precession frequency known as the Larmor frequency (ω_0), as illustrated in Figure 2.1, with

$$\omega_0 = -\gamma H_0 \,. \tag{2.4}$$

In a reference frame rotating about the z-axis (directed along $\vec{H}_0$) at the Larmor frequency, the effective static field is zero and thus $\vec{M}$ appears stationary. When a weak transverse (*i.e.*, in the xy-plane) oscillating field $\vec{H}_1(t) \propto e^{-i\omega_0 t}$ is applied in addition to the static field $\vec{H}_0$, this oscillating field also appears static in the rotating frame, and causes a precession of the magnetic moment about the direction of the oscillating field.

In a typical magnetic field (on the order of a few Tesla), the Larmor frequencies of most nuclei reside in the radio-frequency (rf) range. In nuclear magnetic resonance

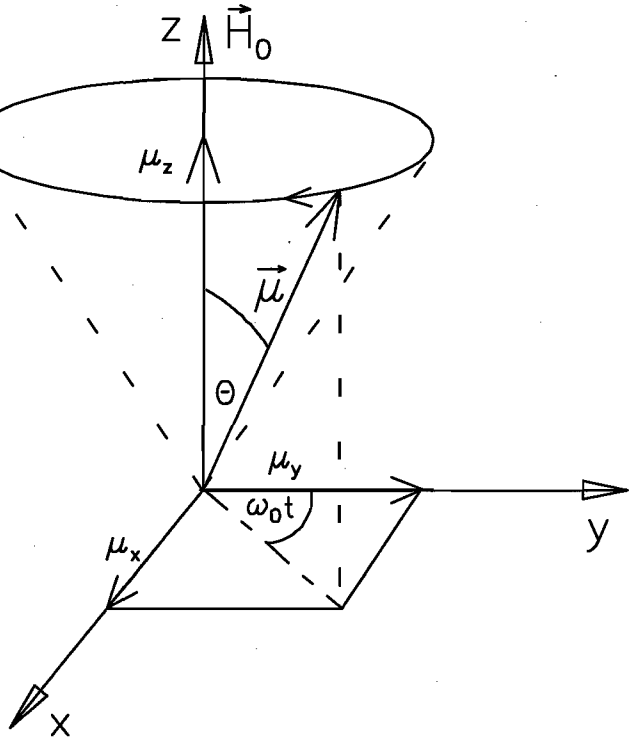

Figure 2.1: Classical view of the precession of a magnetic moment.

this transverse oscillating field is often referred to as the "rf field". If the rf field is applied for a total time t_{rf}, the net angle of rotation θ of the magnetization becomes

$$\theta = \gamma H_1 t_{rf} \, . \tag{2.5}$$

When $\theta = \frac{\pi}{2}$ the magnetization is rotated into the xy-plane from its equilibrium along the z-axis. This is given the name "$\frac{\pi}{2}$ rf pulse".

An equivalent description to the above classical view can be made using quantum mechanics. A nucleus of spin S has $2S + 1$ possible eigenstates of the Hamiltonian

$$\mathcal{H} = -\gamma \hbar \hat{S}_z H_0 \, , \tag{2.6}$$

where $\hat{S}_z$ is the z-component of the spin operator $\hat{S}$. The energy levels of these states are separated by $\hbar\omega_0 = h\nu$ in the presence of an external magnetic field. This effect is called Zeeman splitting (Figure 2.2). For a system in thermal equilibrium with a

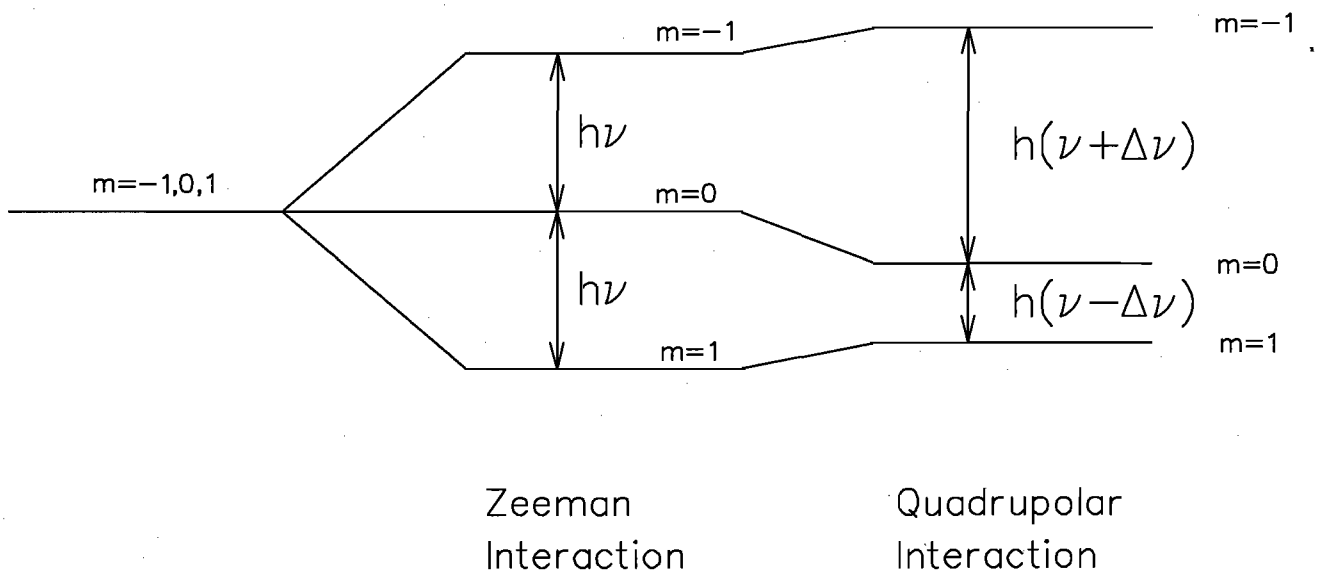

Figure 2.2: Zeeman and quadrupolar splitting.

reservoir at temperature T, the populations of the Zeeman levels are determined by the Boltzmann factors,

$$\frac{N_i}{N_j} = e^{-(E_i - E_j)/k_B T} . \tag{2.7}$$

At this given temperature, the number of spins in the lower energy state (i) is slightly higher than the number of spins in the higher energy state (j). A transverse oscillating field at the Larmor frequency causes transitions between the energy levels, from the absorption of photons. This change in populations causes a change in the net magnetization of the system. Continuous application of an oscillating field will equalize the populations of the two states and de-polarize the system, causing the net magnetization to approach zero. A coherent manipulation of the populations is also possible; a 180° rf pulse will exchange the populations of the two states, causing a flip of the magnetization vector.

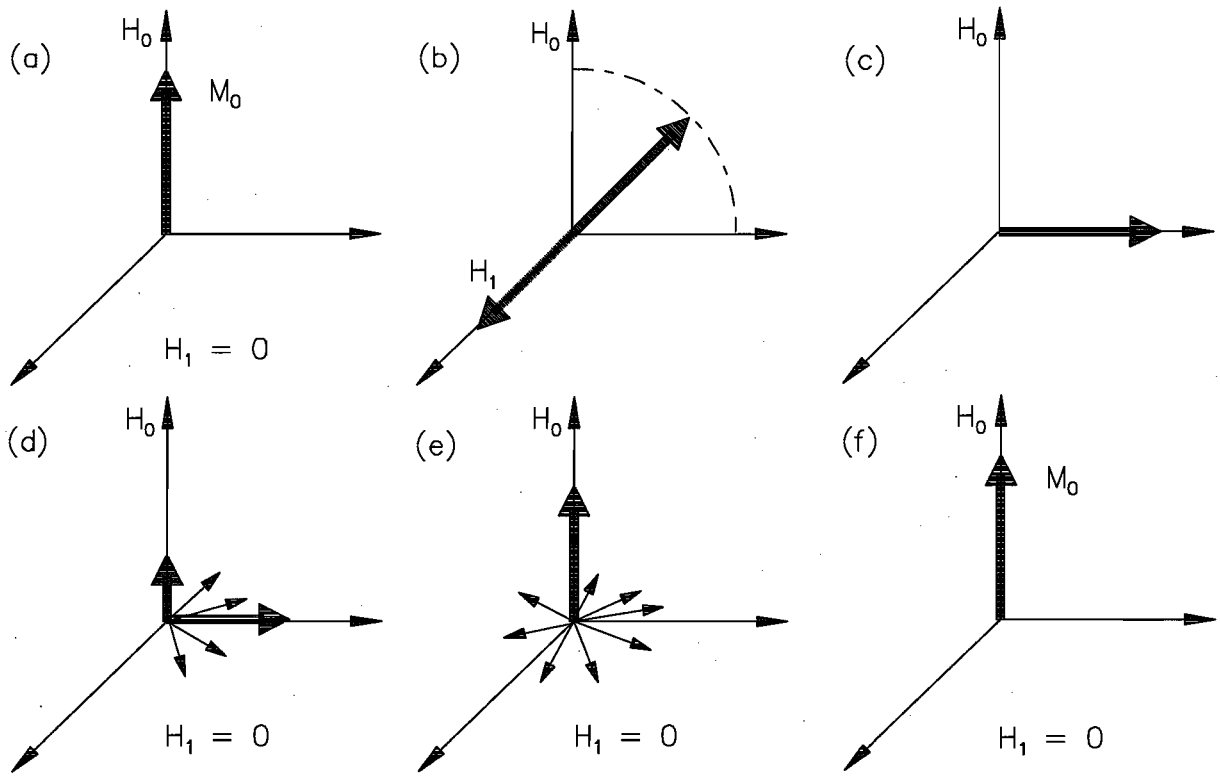

Figure 2.3: Schematic of the spin relaxation mechanism. Figure reproduced from [41].

2.2 Relaxation

Relaxation is observed when the spin system returns to equilibrium after it is perturbed by an rf pulse (the transverse magnetic field H_1). This return to equilibrium is achieved through an exchange of energy between the nuclear spin system and the surrounding molecular environment, referred to as the lattice. This is known as T_1, or spin-lattice relaxation. After perturbation, the z-component of magnetization returns to equilibrium with a time constant T_1.

Transverse relaxation is a form of loss of coherence due to irreversible spin-spin interactions. This transverse relaxation is also known as T_2, or spin-spin relaxation. This relaxation (for a spin $\frac{1}{2}$ system) is illustrated in Figure 2.3. The magnetization vector is initially aligned with H_0 (Figure 2.3(a)). The transverse field H_1 oscillating

at the Larmor frequency ω_0 causes the rotation of the magnetization vector into the xy-plane, as seen in Figures 2.3(b) and 2.3(c). After the transverse field is turned off, $\vec{M}$ starts to precess about H_0. Due to the inhomogeneities in H_0, the Larmor frequencies of different nuclei vary, and $\vec{M}$ fans out, as seen in Figure 2.3(d), leading to the decay of the transverse magnetization and a free induction decay (FID). However, local microscopic magnetic fields fluctuate randomly, causing a loss of phase coherence. This decay is characterized by a time constant T_2. At the same time, the longitudinal component of $\vec{M}$, M_z is growing with a time constant T_1, which is different from T_2 [42], as seen in Figures 2.3(d) to 2.3(f).

2.3 Spin-1 Systems

Spins greater than $\frac{1}{2}$ (for example, the deuterium atom has a spin of 1) possess an electric quadrupole moment which interacts with electric field gradients (EFG) produced by surrounding electron clouds. This small effect shifts the Zeeman levels slightly (refer to Figure 2.2). With a greater quadrupole moment, and a stronger EFG, the shift in energy levels becomes larger.

The EFG is due to the distribution of electronic charge, and thus the principal axis of its tensor is a molecule-bound system. If the z-axis of the principal axis reference frame of the EFG tensor is associated with the direction of the chemical bond ($V_{zz} = eq$), the quadrupole interaction is described by the following Hamiltonian [43]:

$$\mathcal{H}_q = \frac{e^2qQ}{4S(2S-1)\hbar}\left[3\hat{S_z}^2 - \hat{S}^2 + \eta(\hat{S_x}^2 - \hat{S_y}^2)\right] , \tag{2.8}$$

where eQ is the quadrupole moment, and η is the quadrupole asymmetry parameter, $\eta = \frac{V_{xx}-V_{yy}}{V_{zz}}$.

For an axially-symmetric EFG, $V_{xx} = V_{yy}$ and thus $\eta = 0$. For a spin $S = 1$ in

this symmetric EFG, the Hamiltonian reduces to:

$$\mathcal{H}_q = \frac{e^2qQ}{4S(2S-1)\hbar}\left(3\hat{S}_z^{\,2} - 2\right) = \frac{\omega_q}{3}\left(3\hat{S}_z^{\,2} - 2\right) , \tag{2.9}$$

where $\omega_q = \frac{3e^2qQ}{8\hbar}$ is called the quadrupolar frequency. For a C-D bond in a saturated hydrocarbon chain, $\omega_q \approx 2\pi \times 167$ kHz.

To transform the quadrupolar Hamiltonian (Equation 2.8) from the principal-axis of the EFG tensor to the laboratory frame, one can use the Wigner rotation matrices. It can be shown then that the observed quadrupolar splitting is [44]:

$$\Delta\omega_q = 2\pi\Delta\nu = \omega_q\left[(3\cos^2\beta - 1) + \eta\cos 2\alpha \sin^2\beta\right] , \tag{2.10}$$

where α and β are the Euler angles specifying the orientation of the principal-axis reference frame of the EFG tensor in the lab frame. In axially-symmetric cases, the anisotropy depends only on β, the angle between a particular C-D bond and the direction of the external magnetic field H_0,

$$\Delta\omega_q = \frac{\omega_q}{2}\left[(3\cos^2\beta - 1)\right] . \tag{2.11}$$

2.4 Order Parameter

Molecular motions modulate the C-D angle $\beta = \beta(t)$ with respect to the external magnetic field, and influence the observed quadrupolar splitting. The anisotropy is averaged over those motions that are faster than the [quadrupolar] interaction time frame, and it thus appears as a motional narrowing of the signal. The time modulation of the angle $\beta = \beta(t)$ caused by the motions slower than the interaction time frame is not averaged out, but is instead seen as a superposition of signals from multiple β values.

Biomembranes have rapid axially-symmetric reorientational motions about the lipid bilayer normal. Thus it is useful to transform into the lab frame. This is done

in two steps. First, the EFG frame associated with the C-D bond is transformed into the frame associated with the symmetry axis of the lipid molecule; and second, this molecule-bound frame is transformed into the lab frame. The first transformation is described by Euler angles α' and β', and the second transformation is described by the Euler angles θ and ϕ. A time-average taken over the rapidly changing α' and β' yields a single scaling factor, the orientational order parameter (S_{CD}) of the C-D bond,

$$S_{CD} = \frac{1}{2}\left\langle (3\cos^2\beta' - 1) + \eta\cos 2\alpha' \sin^2\beta' \right\rangle , \tag{2.12}$$

where the average $\langle \ldots \rangle$ is taken over the rapid reorientational motions.

In an axially symmetric case, $\eta = 0$, the order parameter reduces to

$$S_{CD} = \frac{1}{2}\left\langle 3cos^2\beta' - 1 \right\rangle , \tag{2.13}$$

where the average is taken over the fast (on the NMR time scale) motions that modulate $\beta'(t)$.

Smaller values of S_{CD} correspond to more disorder, *i.e* to more rapid random reorientations of the C-D bonds. In fully isotropic liquids, $S_{CD} = 0$. In a typical lipid, complex motions possess axial symmetry. This effectively reduces the observed quadrupolar splitting of 167 kHz in the static frame to the 10-20 kHz that corresponds to S_{CD}.

The average over all values of θ and ϕ is a superposition of many individual contributions, this being the observed quadrupolar splitting. The observed quadrupolar splitting is therefore, for a particular value of θ:

$$\Delta\omega_q = \omega_q S_{CD}\left(3cos^2\theta - 1\right) . \tag{2.14}$$

and the average over all possible θ, ϕ is now reduced to the average over θ only, due to the axial symmetry of fast motions. This angle is the one between the axis

of symmetry of the molecule (the normal to the bilayer) and the external magnetic field. The resulting so-called "powder pattern" is expressed in Equations 2.15 - 2.17.

For phospholipid molecules containing many C-D bond sites, a distribution of order parameters $S_{CD}(n)$ is needed. n is the index of the carbon position along the fatty-acid chain of the phospholipid. The carbons at the end of the fatty acid chain move more freely than those close to the phosphate group, and as a consequence, the order parameter tends to decrease towards the terminal methyl group [45]. Phospholipids with shorter fatty acid chains are more ordered and thus exhibit higher average values of S_{CD}. The distribution of quadrupolar splittings in a sample provides a direct measure of the distribution of order parameters, and therefore provides a measure of the range of motional environments available to the various parts of the phospholipid molecule. This allows for an investigation of molecular alignment in the sample, and orientational dynamics.

2.5 Distribution Functions and Powder Spectra

An experimentally observed spectrum is a function of θ, the angle between the molecular axis and the external magnetic field, and the anisotropy parameter $x = \omega_q S_{CD}$. For each value of x (specific to each C-D bond), the observed quadrupolar splitting is related to x through a Legendre polynomial scaling, shown in Equation 2.14 [46]. The observed powder spectrum of a macroscopic sample contains contributions from many x and θ values, so it must be described by both an anisotropy distribution function, $g(x)$, and an orientational distribution function, $p(\theta)$:

$$S(\omega) = \int g(x) \left[p(\theta) \frac{\partial \theta}{\partial \omega} \right] \mathrm{d}x \,, \tag{2.15}$$

$$S(\omega) = \int p(\theta) \left[g(x) \frac{\partial x}{\partial \omega} \right] \mathrm{d}\theta \,. \tag{2.16}$$

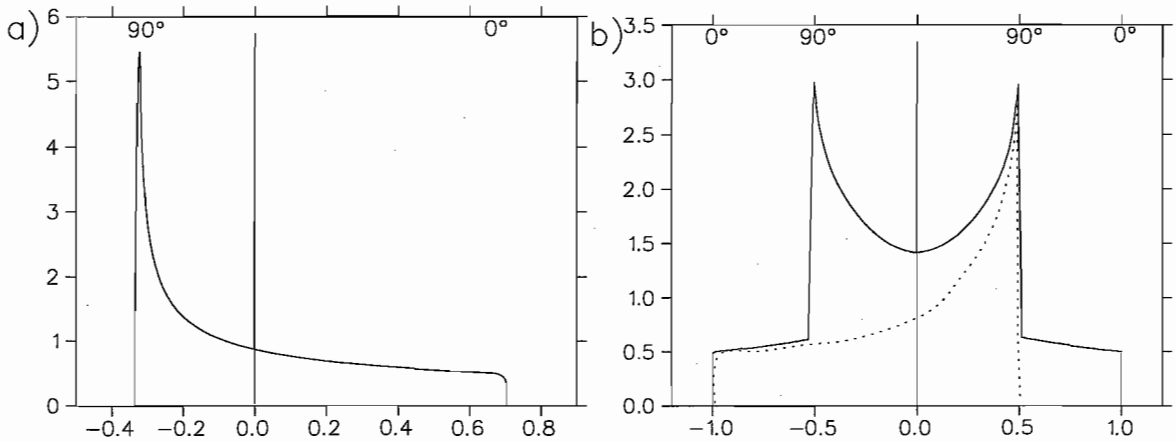

Figure 2.4: Powder Patterns. (a) A general lineshape for spin-$\frac{1}{2}$. (b) Lineshape for spin-1. The spectral lineshape can be thought of as a superposition of two spin-$\frac{1}{2}$ spectra, one for each of the two lines in a quadrupolar doublet. Note a characteristic "peak" in the intensity that corresponds to θ=90°. Figure reproduced from [47].

Equation 2.15 is a $g(x)$-weighted superposition of lineshape functions, one for each anisotropy $x = (\theta, \omega)$, and Equation 2.16 is a $p(\theta)$-weighted superposition of spectra from the individual domains that make up a powder sample, one from each of the orientations $\theta = (\omega, x)$.

For a highly oriented sample, $p(\theta) = \delta(\theta)$. For an isotropic orientational distribution, $p(\theta) \propto \sin(\theta)$ and the lineshape function $p(\theta)\frac{\partial\theta}{\partial\omega}$ can be obtained from Equation 2.14. This is illustrated in Figure 2.4.

$$p(\theta)\frac{\partial\theta}{\partial\omega} = -\frac{p[\theta(x,\omega)]}{[2(x-\omega)(x+2\omega)]^{1/2}} \,. \tag{2.17}$$

Lineshapes such as the one shown in Figure 2.4(b) are called Pake doublets, or Pake patterns, after G.E. Pake [48]. Powder spectra are the superposition of such Pake patterns, with each pattern belonging to a specific carbon position along the fatty acid chain

2.6 De-Pake-ing

Obtaining the distribution of anisotropies $g(x)$ from the experimentally measured spectrum $S(\omega)$ is essentially an inversion of Equations 2.15 and 2.16, and is referred to as de-Pake-ing [49, 50]. Rewriting Equation 2.15 gets

$$S(\omega) = \int g(x)C(x,\omega)\,\mathrm{d}x\,, \tag{2.18}$$

where $C(x,\omega)$ is the kernel function,

$$C(x,\omega) = \begin{cases} p(\theta)\frac{\partial\theta}{\partial\omega}, & \text{for } -\frac{x}{2} < \omega \leq x \\ 0, & \text{otherwise} \end{cases} \tag{2.19}$$

This is a mathematically ill-posed problem. However, several numerical strategies exist for obtaining an approximate solution [51]. If $p(\theta)$ is known, then a traditional iterative algorithm can be used [50]. If $g(x)$ is known, the problem can be solved for an unknown $p(\theta)$, as in the case of the orientational distribution function of a nematic liquid crystal trapped in the channels of a microporous channel [52]. When neither $p(\theta)$ or $g(x)$ are known, Tikhonov regularization can be used to obtain both distribution functions simultaneously [53].

Chapter 3

Neutron Diffraction in the Study of Lipid Bilayer Organization

3.1 Introduction to Neutron Diffraction

The neutron is a neutral elementary particle, discovered by Chadwick in 1932. It is found in all atomic nuclei except for hydrogen. It has a mass of 1.0087 atomic mass units (1.675×10^{-27} kg), a nuclear spin of 1/2 and a magnetic moment [54].

Since neutrons have no charge, their interaction with matter is short-ranged. As a result, neutrons are able to penetrate deeply into condensed matter. The interaction between neutrons and atomic nuclei involves the complex nuclear strong force interactions, including interactions of the nuclear spins and magnetic moments. Because of this, there is no discernible trend in the periodic table of an atom's ability to scatter neutrons. This is in contrast to X-ray scattering, where the scattering factor increases with atomic number. Isotopes of the same element are sometimes found to have different abilities to scatter neutrons. The core principle of neutron scattering arises from the difference in scattering power of the various elements in a sample [54].

In a scattering experiment, the neutron undergoes a change in momentum after being scattered by the atoms in a sample. The neutron's momentum is given by

$$\mathbf{p} = \hbar\mathbf{k}\,, \tag{3.1}$$

where $\hbar = h/2\pi$ is Planck's constant and $\mathbf{k}$ is the neutron wave vector, $|\mathbf{k}| = 2\pi/\lambda$. The wavelength ($\lambda$) is given by

$$\frac{h^2}{2m\lambda^2} = 2k_B T \,, \tag{3.2}$$

where k_B is Boltzmann's constant and T is the neutron moderator temperature.

The change in momentum can be described by the scattering vector $\mathbf{Q}$, which is defined as the vector difference between the incident ($\mathbf{k}_0$) and scattered ($\mathbf{k}_1$) wave vectors,

$$\mathbf{Q} = \mathbf{k}_0 - \mathbf{k}_1 \,. \tag{3.3}$$

The change in the neutron's momentum is given by $\hbar\mathbf{Q}$.

In addition to a change in direction, the magnitude of $\mathbf{k}$ changes, as the energy between the neutron and the sample are exchanged. The law of conservation of energy can be expressed as

$$E = E_0 - E_1 = \hbar^2 \frac{\mathbf{k}_0^2}{2m} - \hbar^2 \frac{\mathbf{k}_1^2}{2m} = \hbar\omega \,, \tag{3.4}$$

where E is the energy gained or lost by the neutron.

When $E = 0$, scattering is completely elastic. It is then required that we have $|\mathbf{k}_1| = |\mathbf{k}_0|$, and putting this into Equation 3.3, one gets $|\mathbf{Q}|=2\mathbf{k}_0 \sin\theta$. In a crystalline material, Bragg peaks appear at values $\mathbf{Q}$ equal to the reciprocal lattice spacing:

$$|\mathbf{Q}| = \frac{2\pi}{d} \,, \tag{3.5}$$

where d is the spacing of set a crystal planes. Since $k_0=2\pi/\lambda$, carrying out the substituions leads to the familiar Bragg equation:

$$\lambda = 2d \sin\theta \,. \tag{3.6}$$

The Bragg equation is the condition of constructive interference of waves with incident angle θ on a set of equidistant planes separated by a distance d.

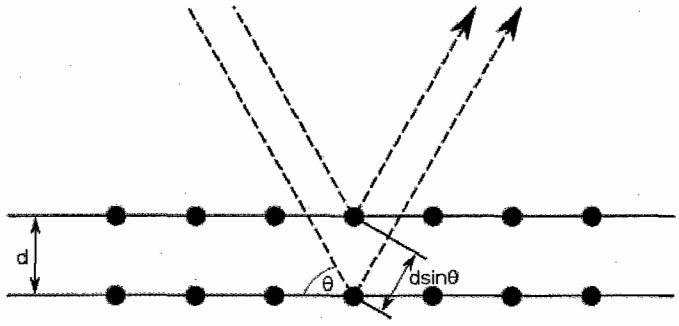

Figure 3.1: Neutrons encounter an atom and are scattered. The horizontal planes of atoms are separated by a distance d. Both the incident and diffracted neutron beams make an angle θ with respect to the planes of the atoms.

A typical neutron scattering experiement involves counting the number of neutrons scattered off atoms in a sample in a particular direction, without regard for any changes in energy. Assuming the distance between the detector and nucleus is large, so that a small angle $\mathrm{d}\Omega$ subtended by the detector is well defined, the differential cross-section can be defined as

$$\frac{\mathrm{d}\sigma}{\mathrm{d}\Omega} = \frac{\text{number of neutrons scattered per second into } \mathrm{d}\Omega}{\Phi\,\mathrm{d}\Omega}\,, \tag{3.7}$$

where Φ is the incident neutron flux. The total scattering cross-section is defined as the total number of neutrons scattered per second in all directions, normalized by the flux:

$$\sigma_s = \int \left(\frac{\mathrm{d}\sigma}{\mathrm{d}\Omega}\right) \mathrm{d}\Omega\,. \tag{3.8}$$

In the case of neutrons being scattered by a single fixed nucleus, the incident neutrons can be represented by a plane wave, $\psi_0 = \exp(i\mathbf{k}_0 z)$. The origin is at the position of the nucleus, and the z-axis is along the direction of $\mathbf{k}$. Since the scattering nucleus is very small, scattered waves emanate from a point source, and the scattering is spherically symmetric. The form of the scattered neutrons at the detector location

of $\mathbf{r}$ is written as

$$\psi_1 = \frac{b}{r} e^{i\mathbf{k}_1 \mathbf{r}} \,. \tag{3.9}$$

The quantitiy b is a measure of the scattering ability of the particular nucleus. It is a constant, specific for each nucleus and is related to the above defined total cross-section. If the incident neutrons have a velocity v, then the number of neutrons passing through a defined area $\mathrm{d}S$ per second is

$$v\,\mathrm{d}S|\psi|^2 = v\,\mathrm{d}S\frac{b^2}{r^2} = vb^2\,\mathrm{d}\Omega \,. \tag{3.10}$$

The flux of the incident neutrons is

$$\Phi = \nu|\psi_0|^2 = v \,. \tag{3.11}$$

Using the definition of neutron cross-section,

$$\frac{\mathrm{d}\sigma}{\mathrm{d}\Omega} = \frac{vb^2\,\mathrm{d}\Omega}{\Phi\,\mathrm{d}\Omega} = b^2 \,, \tag{3.12}$$

and in this case one gets $\sigma_s = 4\pi b^2$ [54, 55]. When neutrons encounter individual nuclei, they are scattered isotropically. Nuclei with non-zero spin are able to interact with neutron spin, leading to a total cross-section with both coherent and incoherent components of the scattering length b.

When a neutron of spin $1/2$ encounters a single isotope with spin I, the spin of the neutron-nucleus system assumes one of two values, $I \pm 1/2$. The scattering lengths of the two systems is then denoted by b^+ and b^-, and the number of spin states associated with each are $2(I + 1/2) + 1 = 2I + 2$ and $2(I - 1/2) + 1 = 2I$, respectively, leading to $4I + 2$ total number of states. If the neutrons are unpolarized and all nuclear spins are oriented randomly, each spin state has the same probability. Then, the frequency of the b^+ and b^- systems are weighted by $(I + 1)/(2I + 1)$ and $I/(2I + 1)$, respectively.

The coherent cross-section for each isotope is given by $\sigma_c = 4\pi\overline{b}^2$, with $\overline{b}$ representing the thermally averaged scattering length with + and - spin state populations. Similarly, the total cross-section is given by $\sigma_s = 4\pi\overline{b^2}$. Using the above, the average coherent scattering length is then defined by

$$\overline{b} = \frac{1}{2I+1}[(I+1)b^+ + Ib^-] \,, \tag{3.13}$$

$$\overline{b^2} = \frac{1}{2I+1}[(I+1)(b^+)^2 + I(b^-)^2] \,. \tag{3.14}$$

The difference between the coherent and total scattering cross-sections leads to the incoherent cross-section

$$\sigma_i = \sigma_s - \sigma_c \,. \tag{3.15}$$

If the atom has no spin, $b^2 = \overline{b}^2 = \overline{b^2}$, and there is no incoherent scattering.

The coherent scattering cross-section contains information on interference effects arising from the structure of a sample. The incoherent cross-section contains no structural information or interference effects, and forms a flat background which must be subtracted from the data. However, the incoherent component does contain information on the motion of single atoms, which are investigated by studying the changes in energy of the scattered beam. The effective total scattering cross-section in the lab is neutron wavelength dependent [54].

Neutron flux from reactors is small. This translates into long experiments to achieve high signal to noise ratios. Contrast variation is used in the determination of the structure and dynamics of biological samples.

The scattering associated with the coherent cross-section has a spatial distribution, a function of the distribution of atoms within the sample. The amplitude of the scattered neutron wave is called the structure factor, defined as

$$S(\mathbf{Q}) = \sum_i = b_i e^{i\mathbf{Q}\cdot\mathbf{r}_i} \,, \tag{3.16}$$

with the sum over all atoms in the sample. The measured intensity of the scattered neutrons is proportional to the square of the structure factor

$$I(\mathbf{Q}) \propto |S(\mathbf{Q})|^2 \,. \tag{3.17}$$

3.2 Reconstruction of the Bilayer

The reconstruction of the bilayer from neutron diffraction data begins with the Bragg peak intensities. The area under each peak is integrated for each order I_h, and corrected for neutron absorption (A), geometry of the beam and sample width (G), and the Lorentz factor (L). These corrections are given by

$$A = \frac{\alpha}{1 - e^{-\alpha}}, \quad \alpha = \frac{2\mu t}{\sin\theta} \tag{3.18}$$

$$G = \sin\theta \tag{3.19}$$

$$L = \sin(2\theta) \tag{3.20}$$

where μ is the calculated absorption coefficient, and t is the sample thickness. The intensities and corrections result in the discrete structure factors $|F_h|^2 = (AGL)I_h$. The corrections affect the different Bragg orders because they depend on the scattering vector $\mathbf{Q}$.

In biological solutions, it is often difficult to resolve individual atoms, and so the concept of scattering length density is employed. Due to each nucleus present having a different scattering amplitude, the scattering length density (SLD) is defined as the sum of the coherent scattering lengths over all atoms within a given volume. This is equated as the Fourier transform of the structure factors,

$$\rho(z) = F_0 + 2\sum_{h=1}^{h_{max}} F_h \cos\left(\frac{2\pi z h}{d}\right) \,, \tag{3.21}$$

with z being the distance along the bilayer normal (z=0 is defined as the centre of the bilayer), and F_0 being the calculated SLD of the entire unit cell, per mole of sample. F_0 is unmeasurable, and therefore an estimated quantity based on chemical composition and an assumption of mass density of the sample.

Because of the differences in scattering cross-sections between isotopes (see Table 3.1), it is common practise to label a specific portion of the sample. Determining the difference between labelled and unlabelled samples, $F_h = F_h^L - F_h^U$ is then easily done so long as the structure factors for both samples are placed on the same relative scale. The difference in SLD profile then reports the location of the centre of mass of the isotopic/isomorphic substitution label, with all other molecular components subtracted away. However, since these represent two different samples, slight difference in sample amount can mean that F_h^L and F_h^U are on different scales. A simple method to re-scale the SLD profiles involves placing the SLD of each sample on the same relative scale by matching inter-bilayer water layers [56, 57]. Once scaled, the SLD can be subtracted to reveal the label distribution profile.

atom	nucleus	b_c (10^{-12} cm)	σ_c (10^{-24} cm^2)	σ_i (10^{-24} cm^2)	σ_{abs} (10^{-24} cm^2)	$f_{X\text{-}ray}$ (10^{-12} cm)
Hydrogen	^{1}H	-0.374	1.76	79.7	0.33	0.28
Deuterium	^{2}H	0.667	5.59	2.01	0	0.28
Carbon	^{12}C	0.665	5.56	0	0	1.69
Nitrogen	^{14}N	0.930	11.1	0	1.88	1.97
Oxygen	^{16}O	0.580	4.23	0	0	2.25
Phosphorous	P	0.513	3.31	0	0.17	4.22
Chlorine	Cl	0.958	11.53	5.9	33.6	4.74

Table 3.1: Bound atom scattering lengths and cross-sections.

Chapter 4

Differential Scanning Calorimetry in the Study of Lipid Phase Behaviour

4.1 Introduction to Differential Scanning Calorimetry

Lipids exist in a number of polymorphic forms as discussed in section 1.1.1, and temperature-induced transitions between these phases readily occur. Differential scanning calorimetry (DSC) is a powerful physical technique, well suited for the thermodynamic characterization of thermotropic phase transitions in both lipid model membranes and biological membranes. A differential scanning calorimeter is used in the measurement of the energy change that occurs as a sample is heated, cooled, or held isothermally, against an inert reference (a sample of comparable thermal mass and heat capacity, which shows no thermotropic events at the temperature range of interest), together with the temperature at which the energy change(s) occur.

The energy change allows for a measurement of the number of phase transitions that occur in the sample, and a measurement of the temperature at which these transitions occur. These measurements allow for the characterization of a material's

melting processes, measurement of glass transitions, and a range of more complex events. One of the advantages of DSC is that samples are very easily encapsulated (usually with little or no preparation), ready to be placed in the calorimeter, so that measurements can be quickly made.

At temperatures far from a thermotropic event, the temperatures of the sample and reference cells change linearly with time, and the temperature difference between the sample and reference is zero. The calorimeter records the difference between the rates of heat flow into the sample and reference cells as (ideally) a straight, horizontal baseline. When a thermotropic event occurs, it then records the change in rate of heat flow into the sample to maintain a temperature differential of zero.

The differential rate of heat flow is either an exothermic or endothermic deviation from the baseline. Once the thermal event is finished, the calorimeter will either re-establish the original baseline, or it will establish a new one if a change in the specific heat of the sample has occured. DSC allows for a plot of differential heat flow as a function of temperature. From such a plot, temperature, enthalpy, and specific heat can be accurately measured [58].

4.2 Operation of the Differential Scanning Calorimeter

A heat flux type calorimeter is one kind of calorimeter used for DSC. It operates under the principle of differential thermal analysis, where both the sample and reference undergo the same thermal cycle, with any temperature difference being recorded. Power is supplied to the heater, and the heating block temperature (T_b in Figure 4.1) is detected and controlled to increase/decrease according to a preset program. The heat flows equally to both the sample and reference, so that their respective temperatures,

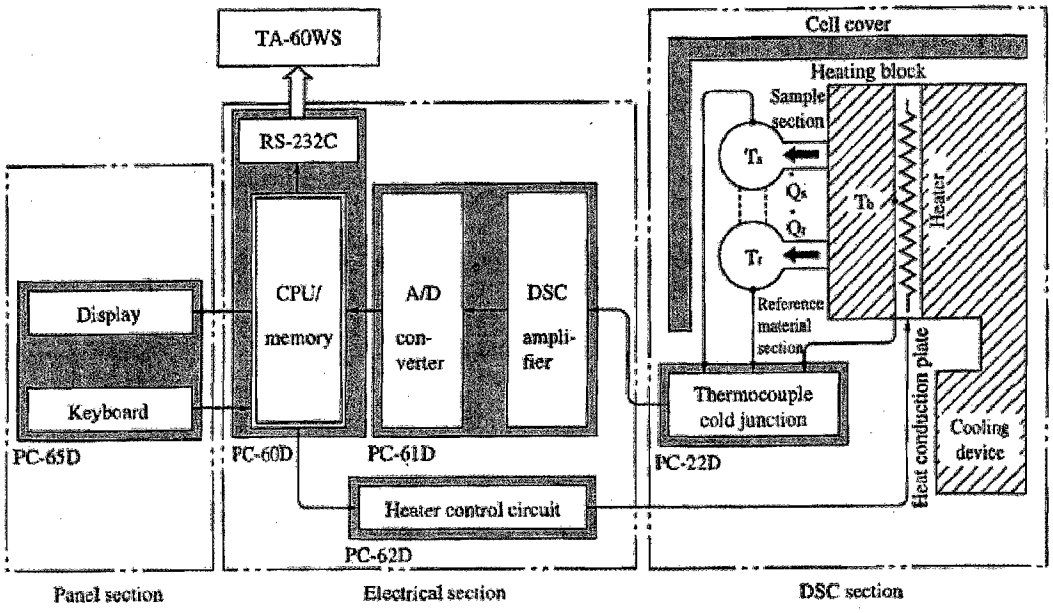

Figure 4.1: The Shimadzu DSC-60.

T_s and T_r increase or decrease after the programmed temperature T_b. At this point the difference between sample and reference temperature is detected as $\Delta T = T_s - T_r$, and forced to zero. ΔP (the differential power) plotted with respect to time is the baseline of the DSC curve. When the sample undergoes a thermotropic event, the sample temperature remains constant while the reference sample temperature continues to rise or fall according to the preset program. As a result, ΔP deviates from the baseline. When the thermotropic event (melting) is complete, the sample temperature is largely different from the heating block temperature. A large amount of heat flows from the heating block to the sample, and the equlibrium state is resumed, and thus ΔP returns to the baseline. This is illustrated in Figure 4.2.

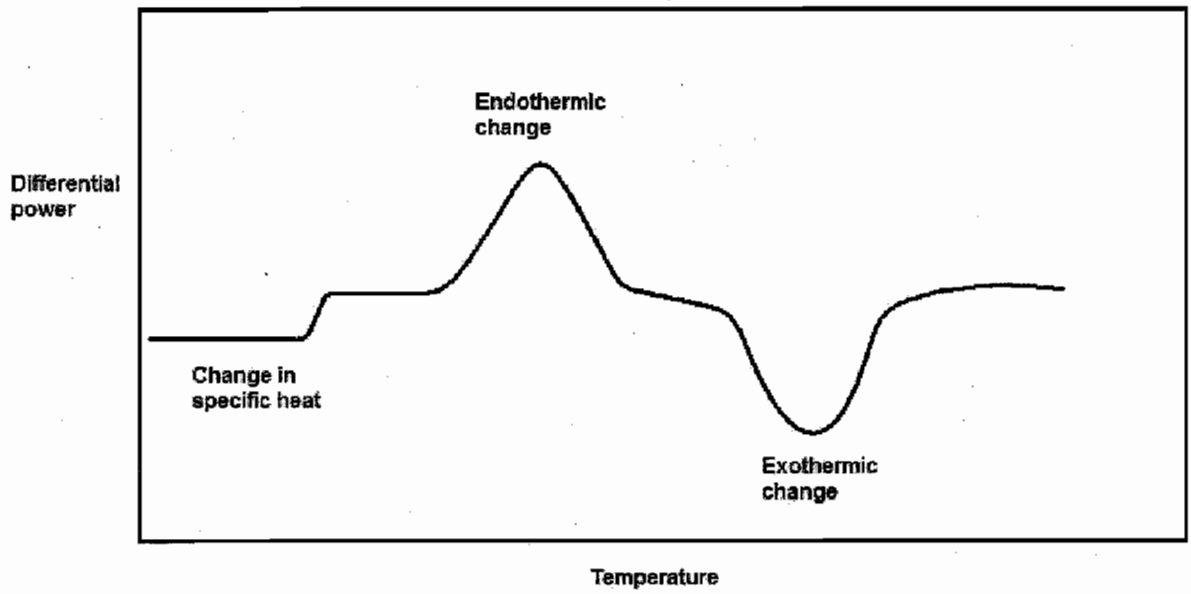

Figure 4.2: A typical DSC curve, showing both endothermic and exothermic deviations from the baseline.

4.2.1 Theoretical Considerations

Statistically, a phase transition can be described as the Boltzman distribution of carbon-carbon (C-C) bond configurations. In the gel phase, the tail group C-C bonds are rigid, in a trans configuration. In the liquid-crystalline phase, the C-C bonds of the tail groups tend to be in a gauche configuration. The distribution of states is given by $w_i = e^{E_i}/k_B T$, where the subscript i represents either the gel or liquid-crystalline state. With an increase in temperature, the liquid-crystalline (E_{lc}) becomes a more probable state for the lipids.

The description of the lipid phase transition is a simple two-state model [58, 59]. The equilibrium constant for this two-state process is

$$K = \frac{[B]}{[A]}\,, \tag{4.1}$$

with [A] and [B] representing the initial and final state concentrations. Assuming volume changes that occur with the thermotropic process are small relative to the total volume, the equilibrium constant can be defined as

$$K = \frac{\alpha}{1-\alpha}\,, \tag{4.2}$$

where α is the fractional conversion, defined as

$$\alpha = \frac{[B]}{[A]+[B]} = \frac{K}{1+K}\,. \tag{4.3}$$

When α is zero, all lipids are in the gel state, and when α is equal to one, all lipids are in the liquid-crystalline state.

The temperature dependence of K is described by the van't Hoff equation,

$$K(T) = K(T_m)exp\left[\frac{-\Delta H_{vH}}{R(\frac{1}{T}-\frac{1}{T_m})}\right], \tag{4.4}$$

where T_m is the transition temperature, or the midpoint of the transition at the temperature where α is equal to 0.5 and $K(T_m) = 1$.

In a DSC experiment, the differential heat capacity c_{diff} is measured as a function of temperature. It is related to the total transition enthalpy Δh_{cal} and the temperature dependence of α through

$$c_{diff} = \Delta h_{cal}(\frac{\mathrm{d}\alpha}{\mathrm{d}T})\,. \tag{4.5}$$

Calculating $\frac{\mathrm{d}\alpha}{\mathrm{d}T}$ from Equations 4.2 and 4.3 and inserting into Equation 4.4 yields

$$c_{diff} = \Delta h_{cal}\left\{\frac{exp[(-\Delta H_{vH}/R)(1/T-1/T_m)]\Delta H_{vH}/RT^2}{(1+exp[(-\Delta H_{vH}/R)(1/T-1/T_m)])^2}\right\}. \tag{4.6}$$

The value of Δh_{cal} is determined from the experimental results by integrating the DSC peak between the temperatures where the baseline deviation occurs,

$$\Delta h_{cal} = \int_{T_{onset}}^{T_{end}} c_{diff}\,\mathrm{d}T\,. \tag{4.7}$$

Δh_{cal} can be converted to the molar transition enthalpy ΔH_{cal} from the known amount of material. This calorimetric transition enthalpy is much lower than the van't Hoff transition enthalpy (ΔH_{vH}) which is calculated from Equation 4.4. The ratio of these two enthalpies ($\frac{\Delta H_{vH}}{\Delta H_{cal}}$) is the cooperative unit, a measurement of how the melting/crystallizing of one lipid affects another lipid [59, 60].

Chapter 5

The Experiments – Materials and Methods

The lipids used in this study, 1,2-dimyristoyl-glycero-3-phosphocholine (DMPC) and its deuterated analog, 1,2-dimyristoyl-d_{54}-glycero-3-phosphocholine (d_{54}-DMPC) were purchased from Avanti Polar Lipids (Alabaster, AL, USA), and used as received. Anhydrous chlorhexidine dihydrochloride and chlorhexidine digluconate were purchased from Sigma–Aldrich (St. Louis, MO, USA), and also used as received. Deuterium-labelled chlorhexidine hydrochloride was synthesized previously [61]. Deuterium-depleted water was purchased from Cambridge Isotope Laboratories Inc. (Andover, MA, USA). HEPES buffer was purchased from Sigma–Aldrich (St. Louis, MO, USA).

5.1 Deuterium Nuclear Magnetic Resonance

Samples were prepared using a protocol established by previous students in the lab. Powder DMPC was dried for several hours under reduced pressure prior to use. Each sample contained approximately 35 mg of lipid, which was mixed with an appropriate amount of a 20% stock solution of deuterated chlorhexidine hydrochloride in deuterium-depleted water. All samples were made under nitrogen atmosphere ($[O_2]$ <2%). Additional deuterium-depleted water was added to bring the total (DMPC+CHX):water ratio to 30:70 by weight. The sample was prepared in a snap-

closure polyethylene container which was then sealed. The molar ratios of the samples prepared were 3:1, 6:1, and 10:1 DMPC:CHX. A pure lipid sample was also prepared. Samples of the same molar ratios, consisting of deuterated DMPC and anhdyrous chlorhexidine dihydrochloride, were also prepared.

Following preparation, the mixing of the samples was achieved by several (at least 5) cycles of freezing in a liquid nitrogen bath followed by thawing in a warm (65°C) water bath. The sample achieved uniform semi-translucent appearance at the end of this procedure. It was then left to equilibrate at 4°C for several days.

All measurements were performed in a 7.0 T Oxford Instruments magnet with a home built spectrometer, using an inductively-coupled probe. Details of the spectrometer design have been reported previously [62]. The temperature in the probe was set and maintained by an airflow temperature controller. Temperature was maintained in each experiment to within ±0.2°C. Samples were allowed to equilibrate for a minimum of 20 minutes between temperature changes. The temperature tended to stabilize to within ±0.1°C of the set point value, and the absolute error of the reported temperature is ±0.5°C.

The ^{2}H NMR experiments were performed at a frequency of 46.061075 MHz. Quadrupolar echo and a modified inversion recovery pulse sequence with varying τ values were used to obtain T_{1z} plots. The time between subsequent scans of the pulse sequence was set at 600 ms for the spectra acquisitions. The dwell time between successive data points acquired by the digitizer was set at 2 μs.

5.2 Neutron Diffraction

Samples were prepared by mixing a stock solution of DMPC in methanol with a stock solution of chlorhexidine dihydrochloride in methanol. The combined sample

was deposited dropwise onto a flat, polished silicon slide, allowing for the solvent to slowly evaporate so as to have uniform sample deposition on the slide. Samples were then placed under vacuum at room temperature for several hours to remove residual solvent. Sample concentrations made were 10:1 and 3:1 DMPC:CHX. Samples were made of protonated lipid and either (1) deuterated, (2) anhydrous, or (3) a salt derivative of chlorhexidine for comparisons.

Neutron diffraction data was recorded at the Candian Neutron Beam centre's D3 beamline, located at the National Research Universal (NRU) reactor (Chalk River, ON), using 2.37 Å wavelength neutrons from a pyrolitic graphite (PG) monochromator. A separate PG filter was used to eliminate higher order (*i.e.*, $\lambda/2$) reflections. During data collection, the sample's temperature was a controlled 36°C, and each sample was hydrated at fixed humidity using saturated salt solutions of KNO_3 (90.8 ± 0.8% relative humidity (RH)), KCl (83.0 ± 0.3% RH), $NaNO_3$ (72.0 ± 0.3% RH), and K_2SO_4 (96.7 ± 0.4% RH), with 70, 16, 8, and 0% D_2O.

5.3 Differential Scanning Calorimetry

Stock solutions of DMPC and chlorhexidine dihydrochloride in chloroform were prepared. Each sample was made by mixing the appropriate amount of stock solutions together to achieve 1.5 mg of lipid with the appropriate ratio of drug in a glass vial. The samples were left under vacuum overnight to allow solvent to evaporate. The samples were then re-hydrated with a 1M solution of HEPES (4-(2-hydroxyethyl)-1-piperazineethanesulfonic acid) buffer (pH 7.46). Each sample underwent 5 freeze/thaw cycles, and then 30 μL of each sample was transferred to an aluminum hermetic pan, and crimp sealed. Ten samples of different molar concentrations of DMPC:CHX (3:1, 5:1, 7:1, 10:1, 30:1, 70:1, 100:1, 200:1, 300:1, 400:1) were

used in the calorimetric study, along with a pure DMPC sample for reference.

Thermograms were recorded using a Shimadzu DSC-60 differential scanning calorimeter. Endothermic thermograms were recorded by heating the samples from 2°C-30°C at a rate of 2°C/minute. Exothermic thermograms were recorded by cooling the samples from 30°C-2°C at a rate of 2°C/minute. Each sample was heated and cooled three times. Values for the transition temperature (T_m), on-set, and end-set of the transition, and the enthalpy (ΔH) were extracted from an average of the three scans.

5.4 Polarized Light Microscopy

Stock solutions of DMPC and chlorhexidine digluconate in ultra-pure water were combined in 10:1 and 3:1 (DMPC:CHX) ratios, for a total solute concentration of 15% (w/w). The samples were put through several vortex/freeze/thaw cycles to ensure thorough mixing and erasing of any lipid thermal phase history. The solution was pulled into a flat-sided capillary (purchased from VitroCom, Inc.), and the ends were flame sealed.

The two samples were examined with polarized transmitted light microscopy using an Olympus BX52 microscope with a temperature controlled stage (Linkam THMS600). The samples were examined from room temperature to 80°C at 5°C/min, and allowed to cool back to room temperature.

5.5 Langmuir Monolayer

To test the lipid affinity of CHX, a small experiment was designed, using a Langmuir monolayer trough (KSV 5000). 0.1 mg of DMPC was spread from chloroform solution onto the surface of ultra-pure water, and the solvent allowed to evaporate off. The

trough barriers were compressed from zero surface tension to 30 mN/m, and the barriers were then set to be continually controlled by the computer to maintain that pressure. After several minutes, ~0.5 mL chlorhexidine digluconate in ultra-pure water was injected into the subphase behind the barriers, on the outside of the DMPC monolayer, to bring the 1 L subphase to 10 μL CHX concentration, well below its 6.6 mM critical micelle concentration. The subphase was not stirred. The subsequent area change due to insertion of the drug was monitored for an additional hour, and any changes were due entirely to diffusion.

Chapter 6

Experimental Results and Discussion

6.1 CHX Has a High Affinity for DMPC

Figure 6.1 shows the polarized light micrographs of DMPC:CHX digluconate at 10:1 and 3:1 ratios, at 26°C. Multi-lamellar vesicles (MLV) are identifiable as the bright circles with dark crosses. There are many large MLV present in the 10:1 sample. In the 3:1 sample, MLV are still present, lesser in quantity and smaller in size. The 3:1 sample is almost entirely characterized by non-lamellar/non-ordered aggregates, reminiscent of images of damaged bacterial plasma membranes. Although there is little lamellar structure observed in the micrographs, one has to note that these samples are in bulk water. The neutron diffraction samples are slightly dehydrated, and deposited on a flat substrate, thereby providing the lamellar alignment needed for diffraction.

With respect to temperature, there was no change in morphology when the samples were heated from room temperature to 80°C. This proves that the membrane disruption caused by CHX is concentration-dependent, rather than temperature-dependent.

The surface activity of CHX has been previously measured, and it was shown to have very little activity at the air/water interface, little penetration into neutral

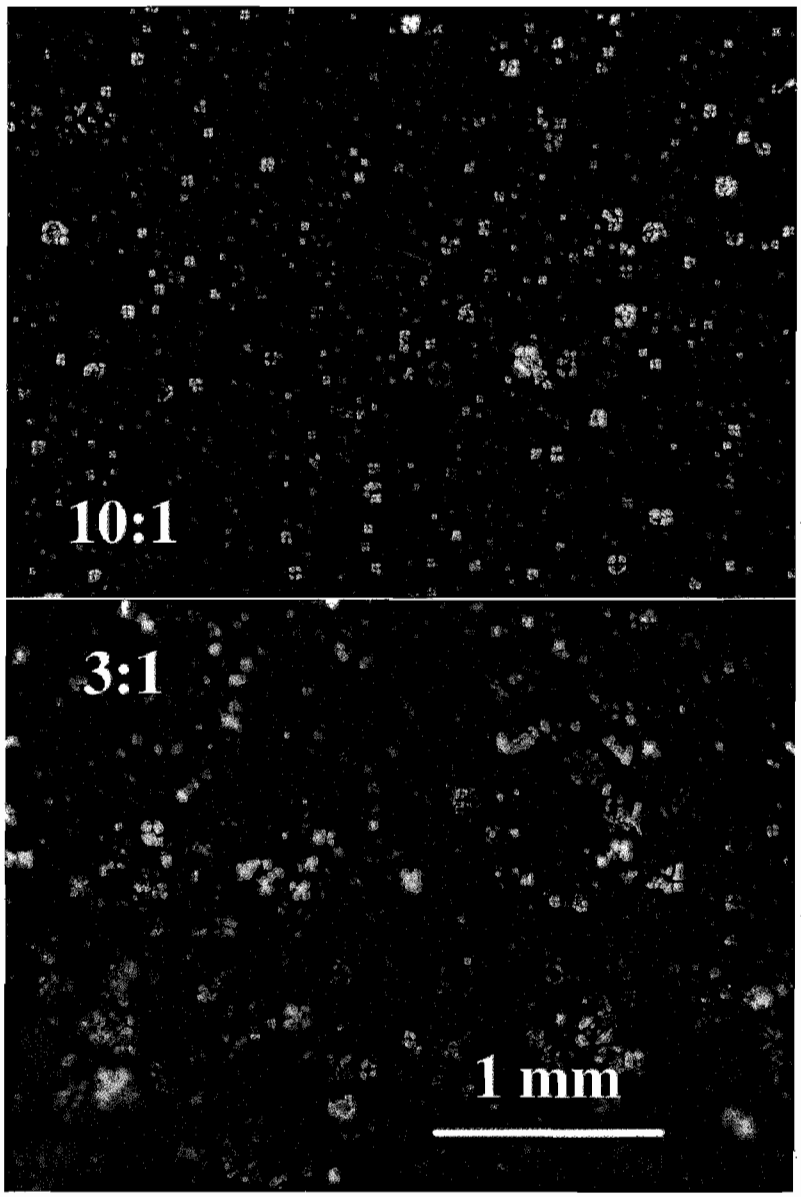

Figure 6.1: Polarized light micrographs of DMPC:CHX at 10:1 (top) and 3:1 (bottom) ratios. Multi-lamellar vesicles (MLV), indicated by the bright circles with dark crosses, are present in both samples. Both images were obtained at 26°C, and showed no variation up to 80°C.

surfactant and lipid monolayers, and preferential insertion into charged surfactant and lipid monolayers [63, 64, 65]. However, these measurements recorded the change in surface pressure at a constant surface area, and in contrast with true surfactant-based antiseptics, CHX cannot insert itself in the monolayer while below cmc in the subphase.

An experiment was designed where the change in surface area is measured, while surface pressure is kept constant. This provided a better model of the membrane damage seen in the effects of CHX on bacteria.

Figure 6.2 shows the slow, but dramatic increase in the surface area of a DMPC monolayer after the injection of CHX digluconate in the subphase. The equilibration regime shows a decrease of 1 cm^2 in the monolayer surface area, over a ten minute period, due to the instabilities of the monolayer over a 1 L subphase. As CHX is injected into the subphase, an immediate surface area increase is observed. Assuming an area per lipid of 60 $Å^2$, the 7 cm^2 increase in surface area represents a 1.5% increase in area per lipid. The drug concentration used was 10 μM; this corresponds to the cmc of CHX since it is in a 1 L subphase. The gluconic acid had little effect at the surface, as it was readily dissolved into the subphase. This result is contrary to previous monolayer results at constant area, but agrees with the first general conclusion that CHX has a strong binding affinity for neutral lipids [65].

6.2 Neutron Diffraction Results

The neutron diffraction experiment was the first in a series of experiments to provide a molecular picture of the interaction of chlorhexidine with a DMPC bilayer. Figure 6.3 shows the typical 4–6 Bragg diffraction peaks recorded. The rocking curves of the first Bragg peak were measured for each sample by rocking the sample around the

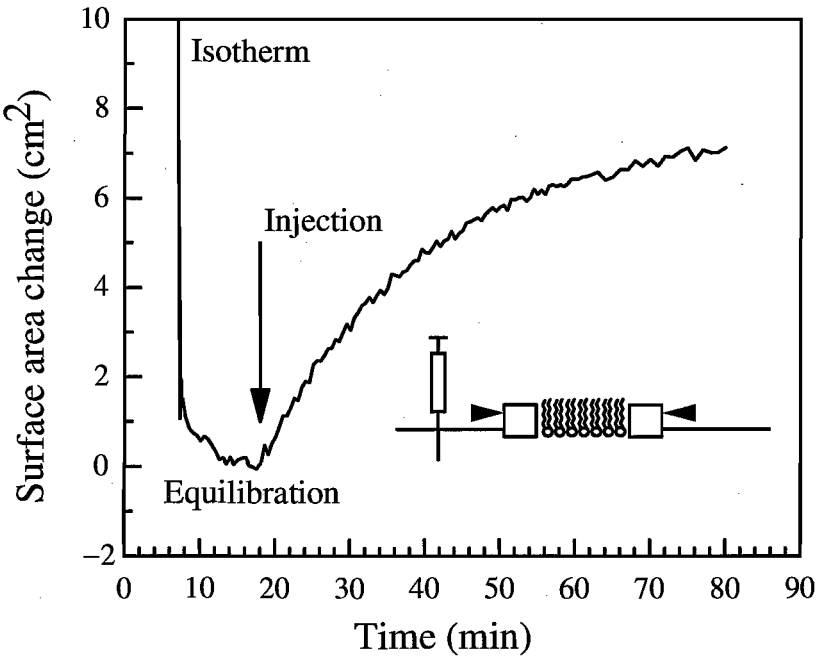

Figure 6.2: The time course of the surface area of a DMPC Langmuir monolayer, adjusted to show the change in area from that at a surface pressure of 30 mN/m. Starting with the initial isotherm, the area slowly decreases from monolayer instability. Immediately following injection of CHX digluconate, the surface area begins to increase without cessation for the next hour.

scattering angle θ, as shown in Figure 6.4. All samples showed reasonable alignment of the bilayer stacks with the substrate, as seen by the sharp peak at θ=0. In the 3:1 samples, a substantial amount of powder diffraction was seen by the very broad ($\pm 3°$), low-intensity background. This indicated that a fraction of the lipids remained in MLV, rather than bilayer sheets, a result that is consistent with the micrograph images. Nonetheless, non-lamellar structures did not contribute in any significant way to the scattering. No amount of annealing was able to improve the sample alignment for the 3:1 samples. Figure 6.5 shows the scattering length density (SLD) profiles

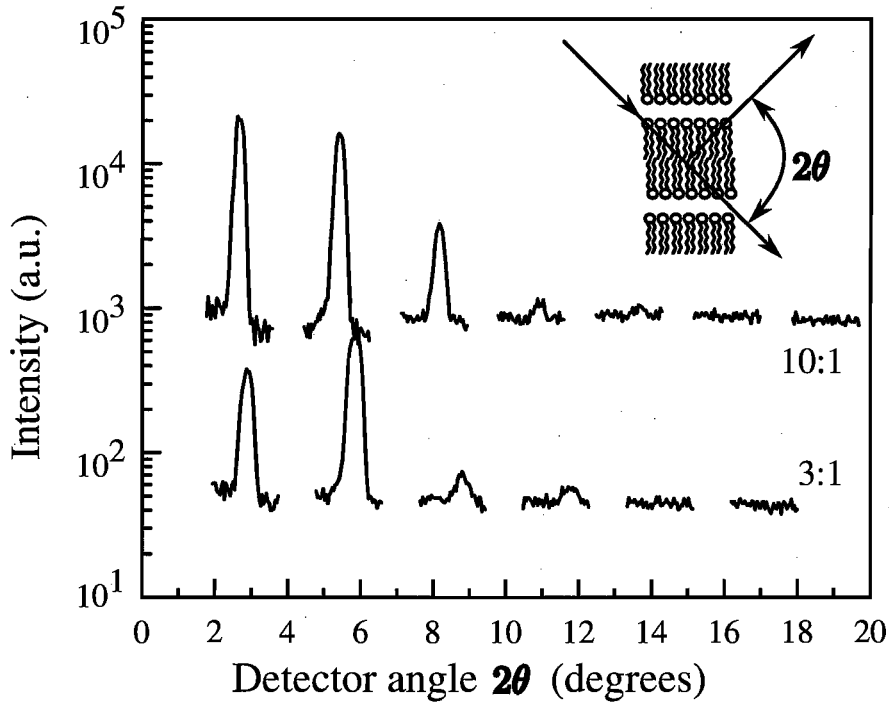

Figure 6.3: Example of raw diffraction data for the 10:1 and 3:1 DMPC:CHX-d8 samples.

of the 10:1 and 3:1 DMPC:CHX-d8 samples at 91% relative humidity, with 8% and 70% D_2O. The illustration of the bilayer is for reference, and to show that the centre of the x-axis corresponds to the centre of the bilayer.

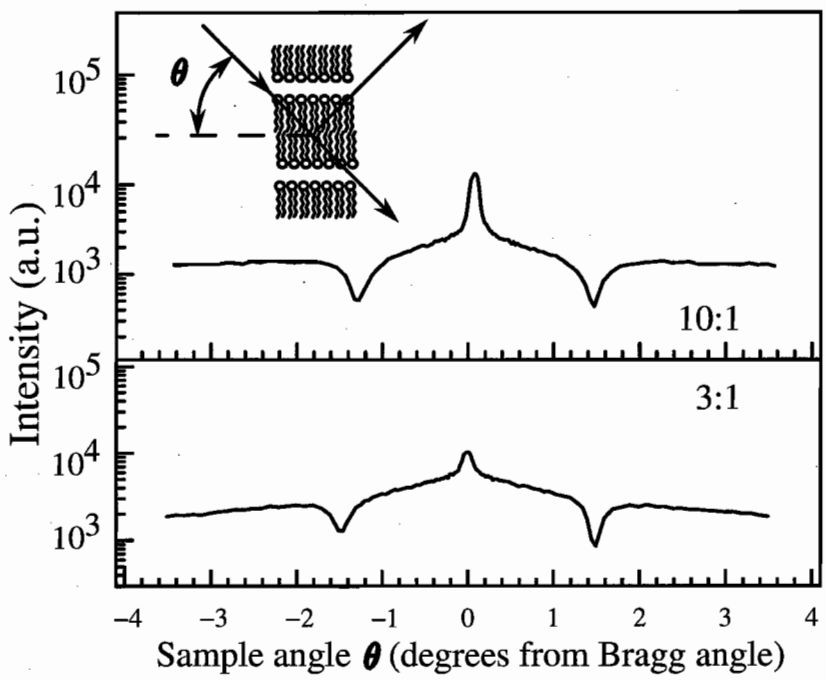

Figure 6.4: Rocking curves of the 10:1 and 3:1 deuterated CHX samples. The dips in intensity seen at $\pm 1.4°$ is when the sample substrate is aligned with the incident and diffracted beams, respectively, where the maximum beam path length through the sample, and thus the maximum absorption, occurs. The broad background, more pronounced in the 3:1 sample, is due to the non-lamellar and non-aligned portion of the sample.

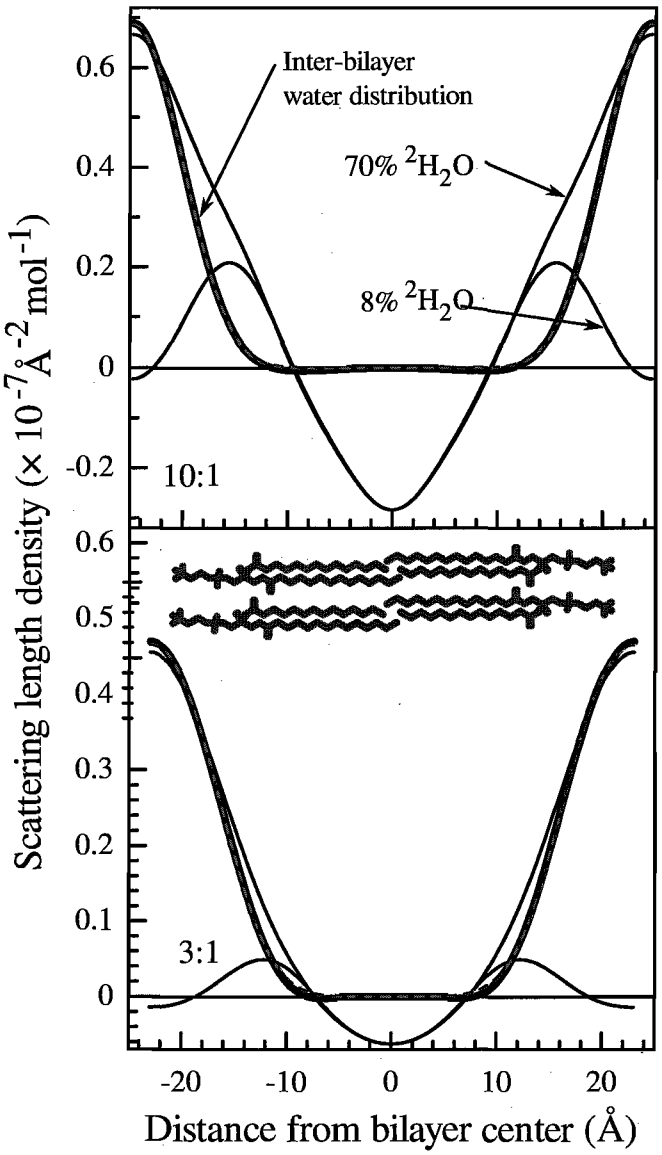

Figure 6.5: The bilayer thickness and water profiles of CHX in DMPC. Shown are the SLD difference profiles between 70 % and 8 % D_2O conditions of 10:1 (upper frame) and 3:1 (lower frame) chlorhexidine in DMPC. The bilayer thickness is defined as the distance between the maxima of the two peaks at ±16 Å (10:1) and ±12 Å (3:1).

The thin lines are the full reconstruction of the SLD profiles, which have been matched at the hexamethylene region exactly. The thick line is the difference between the 70% D_2O and 8% D_2O profiles, and it represents the layer of water between the bilayer stacks. The dashed line is a fit of the water profile to a Gaussian function, representing the water distribution. The distribution of water is modeled well by a single Gaussian centered near the edge of the crystallographic unit cell. It is important to note that by this method of scaling, only the water layers are on an absolute scale, and the bilayer profiles are not (see [66] for why this is so). However, by this method, the deuterated and protonated CHX samples are now on the same relative scale by assuming the amount of inter-bilayer water of the two samples are the same. This should be true since they are compositionally the same (except for the deuterium labelling on the CHX), and at the same temperature and relative humidity.

At a condition of 8% D_2O, the SLD curve is determined strictly by the scattering of the lipid; the total scattering length due to water is zero (refer to Table 3.1 in section 3.2). This SLD curve is characterized by some well-studied features: the negative trough represents the terminal methyl groups at the centre of the bilayer, while the positive peaks at ± 16 Å (10:1) and ± 12 Å (3:1) correspond to a combination of the carbonyl and phosphate moieties. The distance between these positive peaks is used to represent the total bilayer thickness [67, 68].

Figure 6.6 shows the SLD profiles for DMPC samples with deuterated or protonated chlorhexidine introduced. The bold curve is the difference of the two profiles. The dashed curve is a fit of this curve to a single Gaussian, to determine the position, width, and area of the labelled portion of CHX-d8.

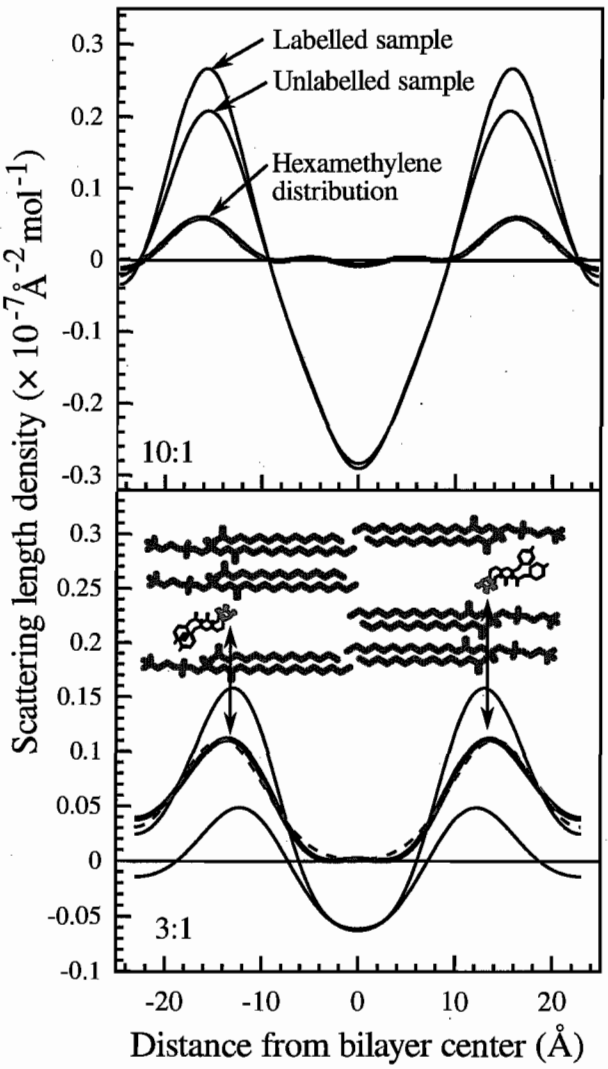

Figure 6.6: Localization of CHX in the bilayer. SLD difference profiles between CHX labelled and unlabelled samples of DMPC:CHX 10:1 (upper frame) and 3:1 (lower frame) chlorhexidine in DMPC. Here the thick line is the time and sample averaged mass distribution of the deuterium atoms in CHX-d8. The bilayer orientation is the same as in Fig. 6.5, and the curves shown are data taken with 8% D_2O, so the inter-bilayer water does not contribute to the profile. Two hypothetical structural arrangements for the CHX are shown; see the text for details.

The distribution of the centre of mass of the deuterium label in CHX-d8 indicates an affinity between the drug and the glycerol backbone of DMPC. In the 10:1 sample, the centre of mass of the deuterium resides 16 Å from the centre of the bilayer, while in the 3:1 sample, the centre of mass of the deuterium resides 14 Å from the centre of the bilayer. In DMPC, this location is precisely between the headgroup and glycerol backbone, as determined by small angle neutron scattering, where the thickness of a DMPC bilayer was found to be 38.3 Å at physiological temperature [39]. The bilayer is proportionally thinner in the 3:1 sample, so the hexamethylene is at nearly the same location relative to the lipid in this sample as in the 10:1 sample.

The width of the distribution is an indication of the time- and sample-averaged mass distribution of the deuterium label. The distribution width for the 3:1 sample is twice that of the 10:1 sample, indicating a few important molecular facts. If the molecular configuration of CHX is the same in both samples, then there is less constraint on the molecular motion of CHX at higher concentrations. This may be a consequence of the increased bilayer disorder seen in the micrographs of Figure 6.1 and the sample mosaic of Figure 6.4. Alternatively, the hexamethylene may be in a straight-chain, extended configuration in the direction normal to the bilayer plane at higher concentrations. However, this alternative raises an important question of why CHX remains at the same penetration depth in the bilayer.

As explained in section 1.4, CHX is amphiphilic in nature, having a hydrophilic component in the aromatic rings and urea chain, and a hydrophobic component in its hexamethylene chain. Free energy is minimized when the hexamethylene is away from water, and the chlorophenol rings are in the vicinity of the hydrophilic headgroup region of the lipid. The presented neutron scattering data shows the centre of mass of the deuterated CHX to lie at the junction of the lipid headgroup and the glycerol babckbone. From this, a few different structural arrangements whereby the

hexamethylene is lifted high towards this junction can be discussed in determining the correct configuration of CHX in the bilayer.

First, if CHX were extended along its hexamethylene chain, the molecule can assume one of a few stretched, straight configurations. The first configuration would be transmembrane (see Figure 6.7). However, a fully extended chlorhexidine molecule is only 28 Å long. With the centre of mass at the headgroup/backbone junction, the CHX molecule would be extended off-centre from the DMPC bilayer, allowing the aromatic ring from one side of the CHX to interact with the hydrophobic tail groups of DMPC, a highly energetically unfavourable configuration. Instead, CHX could lay flat, perpendicular to the normal of the bilayer, "swimming" within the junction. Again, there would be several conflicting interactions in this case. Although the aromatic rings, amines, and hydrophobic hexamethylene are at roughly the same depth, it's difficult to see how they can each possess favourable lipid and water interactions simultaneously. Furthermore, a flat configuration presents difficulties in steric packing, since CHX would displace the lipid headgroups to a great extent. Additional straight-chain, extended configuration possibilities include the favourable interaction of the phenol aromatics through π-stacking. One explanation of the hexamethylene appearing to be lifted so high in the bilayer is that one CHX molecule reaches across the water layer to another CHX from the opposing bilayer, and links via π-stacking. The dimensions of our data seem agree with this; the distance from hexamethylene location to the edge of the unit cell is about 9 Å, which is just short enough to be spanned by the length of the biguanide and phenol ring.

However, the energetics argue against this situation. First assume that two CHX are "shaking hands" with their phenol rings across the inter-layer water. Consider the thermal undulations of the bilayers, whose amplitudes can be on the order of 2-4 Å, despite DMPC's high bending rigidity [69]. This is confirmed in our data by

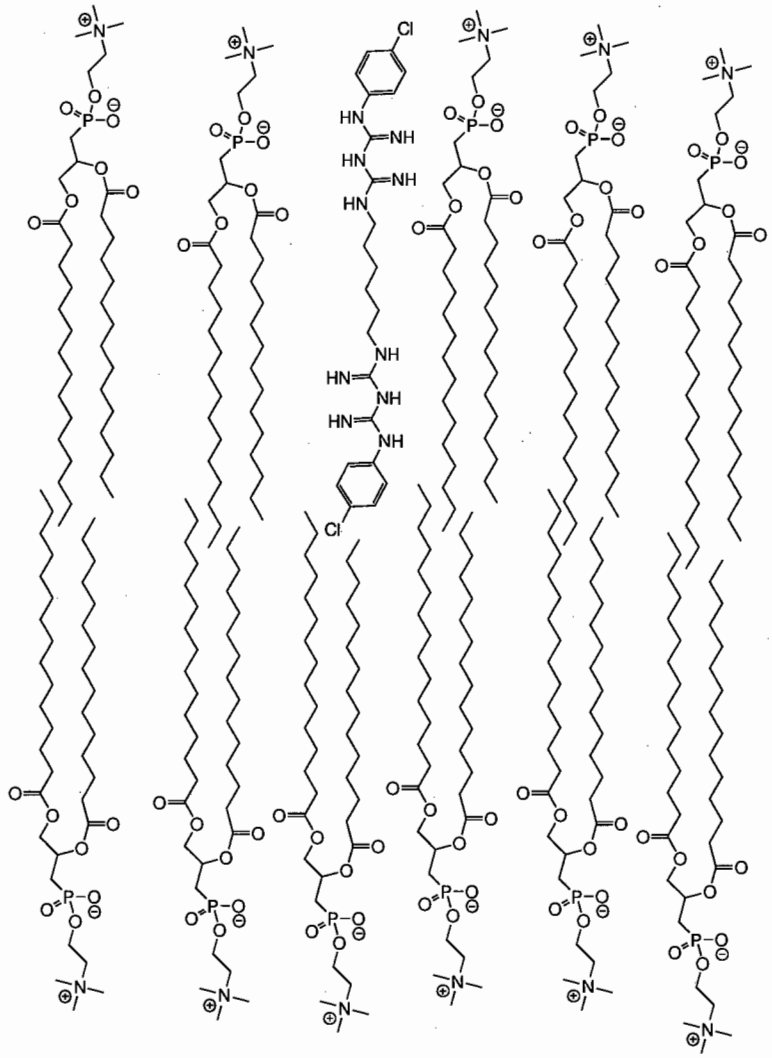

Figure 6.7: One possibility of CHX configuration within a lipid bilayer - extended, and transmembrane through the bilayer.

the width of the Bragg peaks; by using the instrumental resolution, $\delta q_i = 0.011^{-1}$, to de-convolute the inherent peak width, which is related to the correlation length, $\delta q_0 = 2\pi/l$, which we estimate to be on the order of 10 bilayers [70]. This value is small compared to more well aligned samples, indicating large fluctuations. Furthermore, the width of the difference profile of the CHX label, *i.e.* the width of the label mass distribution, is accurate to angstrom resolution [71]. In other words, the time- and sample-averaged fluctuation amplitude of the CHX hexamethylene is 4-6 Å.

Taken together, these fluctuations mean that inter-layer linking of CHX would at some time likely lift one or both hexamethylene completely free of the bilayer. The energy of transfer of a methylene group from organic solvent to water is ~ 8 calmol^{-1} Å^{-2}, or about 1 kcal mol^{-1} for the whole hexamethylene [72]. However, the quadrupole-quadrupole interaction of π-stacking is not much more energetically favourable ($\leq$ 2 kcal mol^{-1}), and decreases with a separation distance as r^{-5} [73]. Thus, the root-mean-squared distance between two phenol rings must be less than 1 Å to have much effect. Therefore, it seems that any handshake between two molecules will be unlikely to form, and those that do will be quickly torn apart.

Rather than an extended configuration, another possibility is for CHX to bend hairpin-like, at the centre (see Figure 6.8). It is well known that the ends of random chains are likely to find each other, and in this case, the folded configuration will be stabilized by intra-molecule π-stacking. This configuration for CHX would mean it creates a point of cleavage in the lipid bilayer. Chlorhexidine would be bent on a central axis, providing the chance for the hexamethylene chain to be near the lipid tail groups, while allowing the urea and aromatics to be interacting with the headgroups, and sticking out into the water outside of the cell. This would seem to be a structurally stable configuration of the drug, and the cleaving is a likely scenario to explain the biocidic properties of the drug. This is quite unlike more

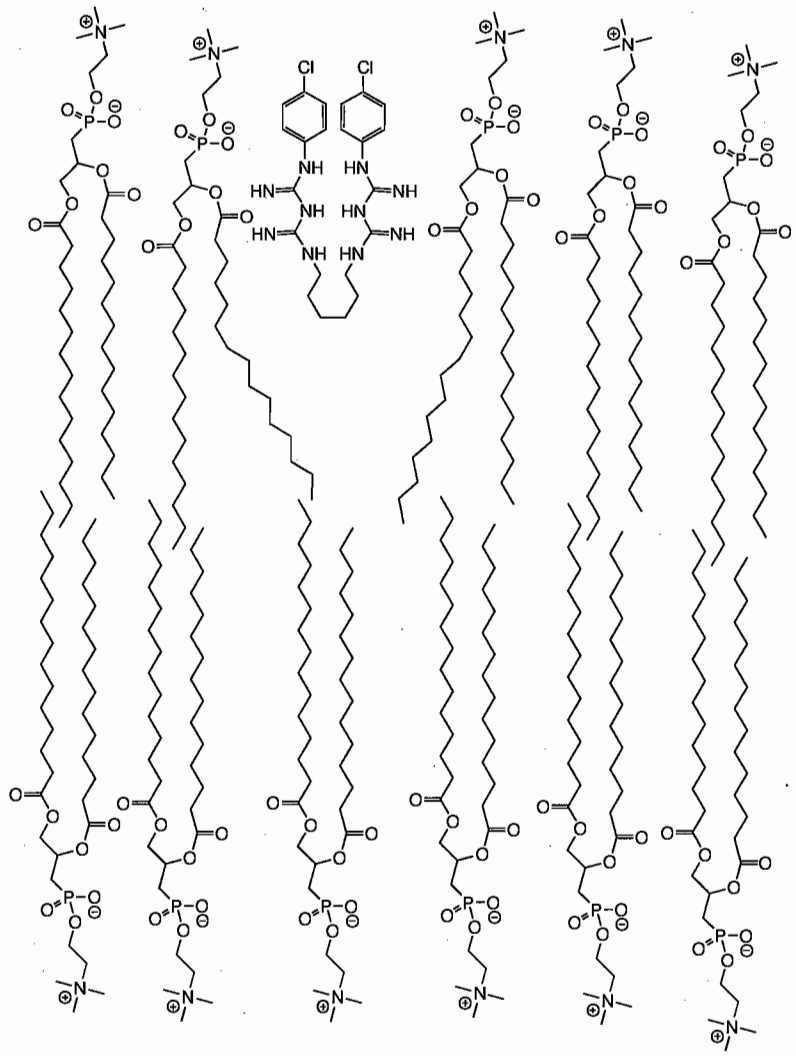

Figure 6.8: Another possibility of CHX configuration within a lipid bilayer - bent hairpin-like on its centre hexamethylene.

obvious surfactant antiseptics such as the quaternary ammonium compounds (QAC), whose acyl chains deeply penetrate into the hydrophobic domain. QAC's detergent-like action on lipids dissolves the membrane and compromises its structure. CHX is more similar to the oblique insertion of helical, amphipathic peptides into membranes, which has been discussed previously as a critical mechanism for fusion and membrane disruption [74, 75]. This idea is not based on amino acid sequence, but rather that a balance of hydrophobicity across the peptide surface is used as a functional device, to insert a wedge into the lipid matrix. The extraordinary amphiphilic nature of CHX might possess similar hydrophobicity patterns if it is in a folded configuration.

The comparison of the 10:1 and 3:1 samples show the bilayer thickness shrinks in the 3:1 sample by more than 8 Å. This is consistent with an expected increase in effective area per headgroup associated with additional cleavage points appearing at the lipid-water interface. This is in agreement with antimicrobial peptides, where membrane thinning is a concentration-dependant effect of the peptide adsorbed into the headgroups [76].

Membrane thinning also occurs with the digluconate samples, as seen in Figure 6.9. No deuterium label discovery could be made with these samples, as deuterated CHX with gluconic salt was not available. However, two observations can be made from the data. The gluconic acid is still present in the aqueous parts of the sample, most likely due to there being not enough inter-bilayer water to dissolve it. We first see that the unit cell size and bilayer thickness is reduced from the anhydrous samples. More interestingly, the inter-bilayer, non-lipid density distribution shows much more penetration into the bilayer headgroups than expected. One can see a pronounced extra "hump" in the 70% D_2O SLD profiles in Figure 6.9 located as deep as the glycerol backbone. Instead of representing just the water, as in the other samples, it is likely a combination of gluconic acid and water.

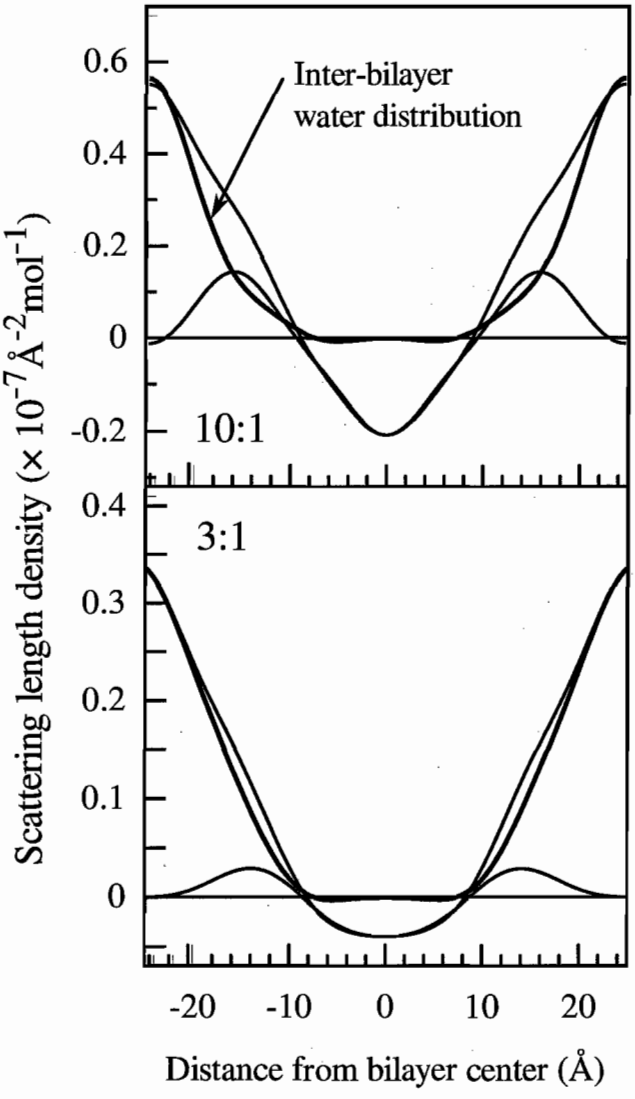

Figure 6.9: Effect of CHX-digluconate on DMPC. Shown are the SLD difference profiles between 70% and 8% D_2O conditions of DMPC:CHX 10:1 (upper frame) and 3:1 (lower frame).

6.3 Differential Scanning Calorimetry Results

The main transition temperature of the gel-to-liquid crystalline phase was studied using differential scanning calorimetry. Ten samples of varying chlorhexidine concen-

tration, and a reference pure DMPC sample were subjected to multiple heating and cooling processes to observe the trend of main transition temperature (T_m) versus increasing drug concentration.

Figures 6.10 and 6.11 illustrate the influence of an increasing chlorhexidine concentration on the main transition temperature of DMPC. The endothermic data of figure 6.10 is an average of the scans taken during the heating runs from 2–30°C. The exothermic data of figure 6.11 is an average of the scans taken during the cooling runs from 30–2°C. The specific values recorded for all scans are outlined in Tables 6.1 and 6.2.

It is quite obvious that an increase in chlorhexidine concentration affects the T_m of DMPC. At the very low concentrations of CHX (far from cmc), there is a small linear change in the transition temperature. However, at the onset of cmc, the T_m of DMPC is drastically reduced, by approximately 10°C. This is not an anomolous trend. Using a sample preparation like our own, Różycka-Roszak and Przyczyna studied the transition temparature of DPPC (dipalmitoylphosphatidylcholine), interacting with a variety of common surfactants. The surfactants tested were N-dodecyl-N,N-dimethyl-N-benzylammonium halides. It was observed that the main transition broadens and shifts progressively to lower temperatures with an increase in surfactant concentration [77]. This broadening is attributed to the benzyl group in the surfactant and occurs at the onset of cmc. The extent to which the transition temperature is shifted was determined by the halide in the surfactant. From this, we note that chlorhexidine has two benzene rings with chlorine attached to them, a similar molecular configuration to the surfactants used in the study done by Różycka-Roszak and Przyczyna [77].

In other studies [78, 79], it was found that the benzyl group of surfactants is easily embedded within micelles, at a location more or less parallel to the surface of the micelle. This result is extended to the insertion of the surfactant in MLV. This

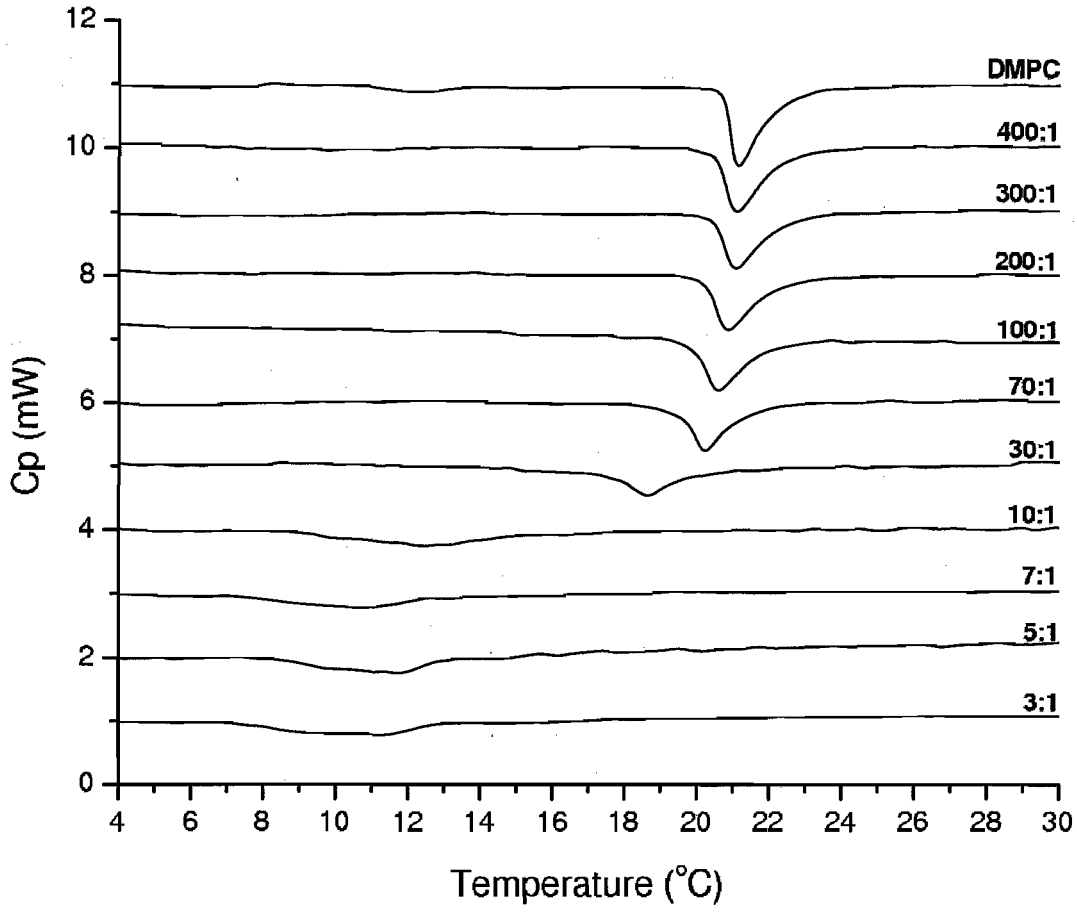

Figure 6.10: Endothermic thermograms of DMPC subjected to increasing concentrations of chlorhexidine dihydrochloride. Scans were recorded from 2°C–30°C in increments of 2°C/min.

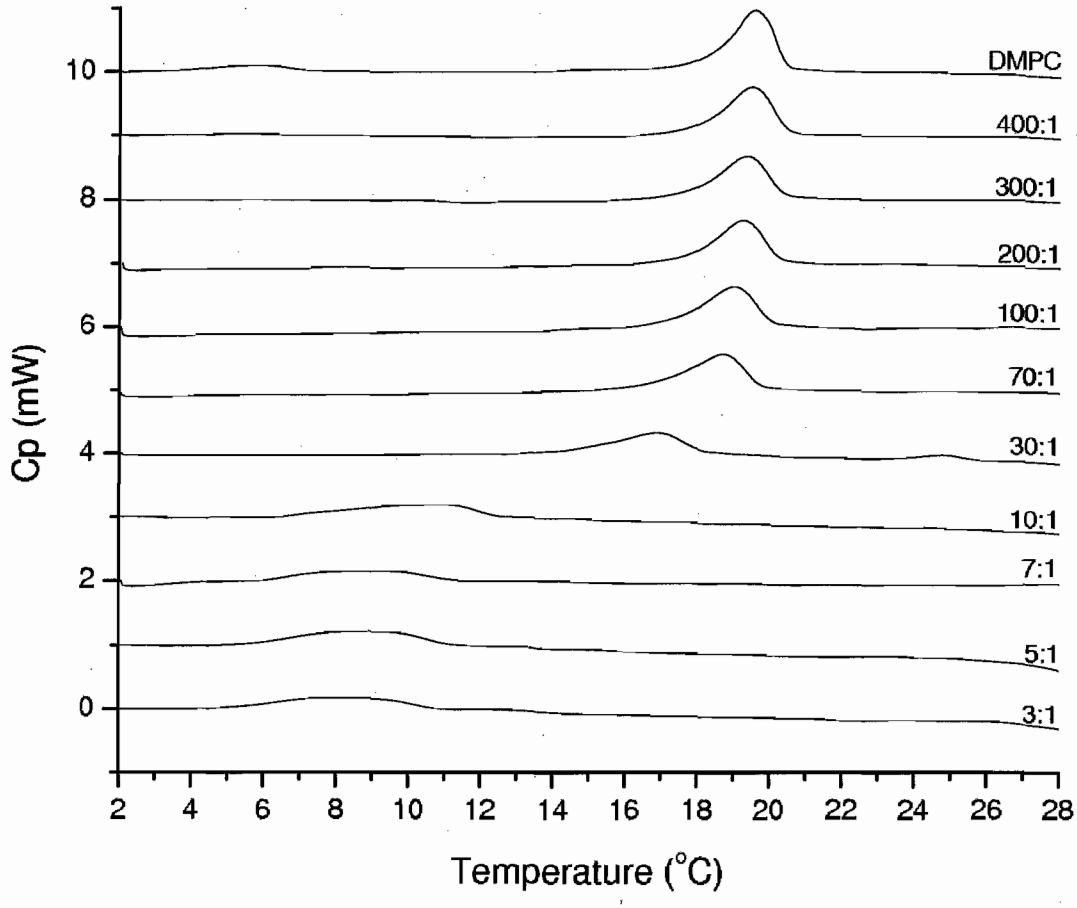

Figure 6.11: Exothermic thermograms of DMPC subjected to increasing concentrations of chlorhexidine dihydrochloride. Scans were recorded from 30°C–2°C in increments of 2°C/min.

is in direct agreement with our neutron data, where it is suggested that the benzene ring of chlorhexidine is situated parallel to the bilayer normal.

In Figures 6.10 and 6.11, a small pretransition is noticed in the pure lipid samples. This pretransition corresponds to the transition between the L'_β (lamellar) and P'_β (ripple) gel phases. It is observed that this pretransition is erased as soon as chlorhexidine is introduced, even at the smallest concentration used. D'Angelo *et al.* [80] observed this when studying DMPC, with the introduction of gramicidin, an antibacterial peptide, and Pignatello *et al.* [81] also observed this same trend, studying the effects of amphiphilic prodrugs on DMPC. In both studies, the pretransition suddenly disappears with the introduction of low concentrations of the additives in question. The pretransition is attributed to the rotation of the lipid headgroups and to the changes in the packing of the hydrophobic tail groups. The pretransition is very sensitive to the presence of foreign additives, as noted by the above mentioned studies, and as noticed in our own. The depression, and disappearance of the pretransition indicates that the additive interacts with the polar region of DMPC, and it alters the preference of the tail groups movements [81].

The area under each curve in the thermograms represents the enthalpy of the transition. For the endotherms, this enthalpy is the amount of heat required for chain melting from gel-to-liquid crystalline phase. For the exotherms, this value is the amount of heat given off from the 'freezing/crystallizing' of liquid crystalline-to-gel phase. The enthalpy is observed to decrease when chlorhexidine concentration is increased. This trend is also noted in previous studies of polycyclic aromatic hydrocarbons and DMPC by Librando *et al.* [82], and studies of chlorhexidine and nonionic tenzides with DPPC done by Szögyi *et al.* [83].

Two other thermotropic values were also noted to be affected by an increase in the drug concentration. The width of the enthalpy peaks broadened by a factor of 3.5

Ratio DMPC:CHX	Fraction	T_m (°C)	δT_m (°C)	Width (°C)	δWidth (°C)	ΔH J/g	$\delta\Delta H$ J/g
Pure	0.0000	21.15333	0.34641	1.56	0.32	31.46	0.57
400:1	0.0025	21.10333	0.34642	1.85	0.09	27.42	1.66
300:1	0.0033	21.10000	0.34641	1.83	0.05	23.43	0.35
200:1	0.0050	20.90000	0.34643	1.86	0.11	24.26	0.67
100:1	0.0099	20.57333	0.34641	1.97	0.23	24.21	0.94
70:1	0.0141	20.20000	0.28284	1.64	0.44	23.03	0.44
30:1	0.0323	18.52333	0.34647	2.62	0.37	20.34	1.64
10: 1	0.909	12.88667	0.34679	4.80	0.76	20.26	0.20
7:1	0.1250	10.97333	0.34664	4.33	0.52	15.20	1.07
5:1	0.1667	11.52500	0.33530	4.96	0.57	14.89	0.20
3:1	0.2500	11.18000	0.34661	5.21	0.59	14.76	1.01

Table 6.1: Transition temperature, peak width, and enthalpy data recorded from the endothermic DSC scans.

from low to high drug concentration (an observation noticed in the studies of [80, 81]), and the cooperativity unit, a value representing the ratio of the van't Hoff enthalpy to the molar transition enthalpy, was also observed to decrease.

Ratio DMPC:CHX	Fraction	T_m (°C)	δT_m (°C)	Width (°C)	δWidth (°C)	ΔH J/g	$\delta\Delta H$ J/g
Pure	0.0000	19.78667	0.34641	1.58	0.02	30.14	1.36
400:1	0.0025	19.65000	0.0.28284	1.92	0.13	28.78	0.81
300:1	0.0033	19.52333	0.34641	2.11	0.11	26.25	0.96
200:1	0.0050	19.42667	0.34641	2.27	0.03	24.41	0.91
100:1	0.0099	19.14000	0.34641	2.46	0.17	24.76	0.38
70:1	0.0141	18.91000	0.28284	2.40	0.37	24.76	0.44
30:1	0.0323	16.94500	0.28284	3.52	0.59	17.56	0.32
10: 1	0.909	10.81333	0.34688	5.45	0.41	16.73	1.12
7:1	0.1250	9.50333	0.34648	4.31	2.24	12.60	0.85
5:1	0.1667	9.18333	0.34714	4.91	0.44	18.81	2.83
3:1	0.2500	8.32667	0.34777	5.58	0.17	15.64	1.18

Table 6.2: Transition temperature, peak width, and enthalpy data recorded from the exothermic DSC scans.

6.4 Deuterium NMR Results

6.4.1 DePaked Spectra and Orientation of Samples

The spectra of the pure DMPC sample are illustrated in Figures 6.12 and 6.13. The two central peaks in each spectra represent the terminal methyl group of the DMPC tails. The dePaked spectra of Figure 6.13 is a plot of the order parameters of the DMPC molecule. Each peak represents the time-average over the rapid molecular motions of each CH_2 group, and the terminal methyl. With an increase in temperature, the spectra are observed to narrow, indicating that the molecular motions are increasing. In the liquid-crystalline phase, the DMPC tail groups are very flexible,

and an increase in temperature simply means that the trans-gauche isomerizations (flexing, kinking, *etc.*) are occuring more often.

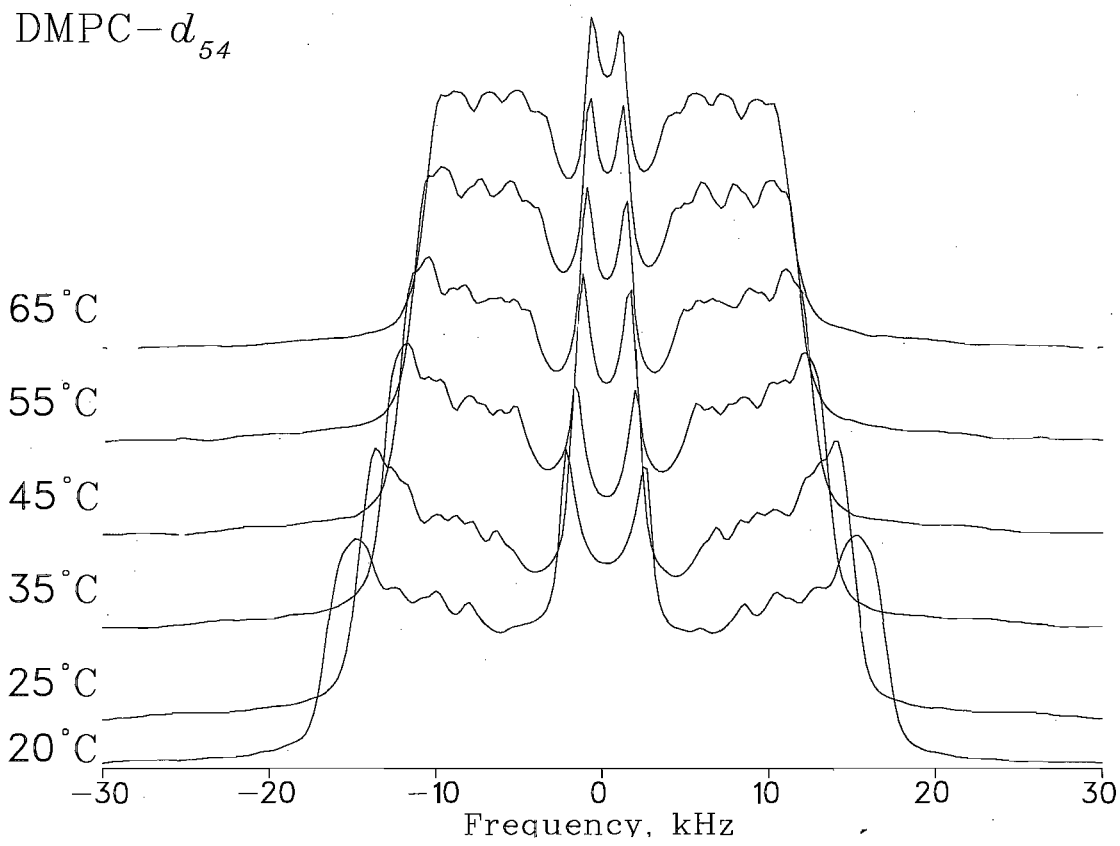

Figure 6.12: Spectra of the pure DMPC sample at various temperatures.

Following the pure sample, a series of lipid/drug formulations were subjected to quadrupolar echo measurements, again at a range of temperatures.

Compared to the pure sample, each subsequent sample had less deuterium atoms in it. The pure sample was a ratio of 30% lipid to 70% water by mass. The samples studied by NMR were 10:1, 6:1, and 3:1 samples of DMPC-d_{54}:CHX and DMPC:CHX-d_8. A calculation of signal strength of each sample compared to the pure sample was done to determine the number of scans necessary to acheive the same signal-to-noise

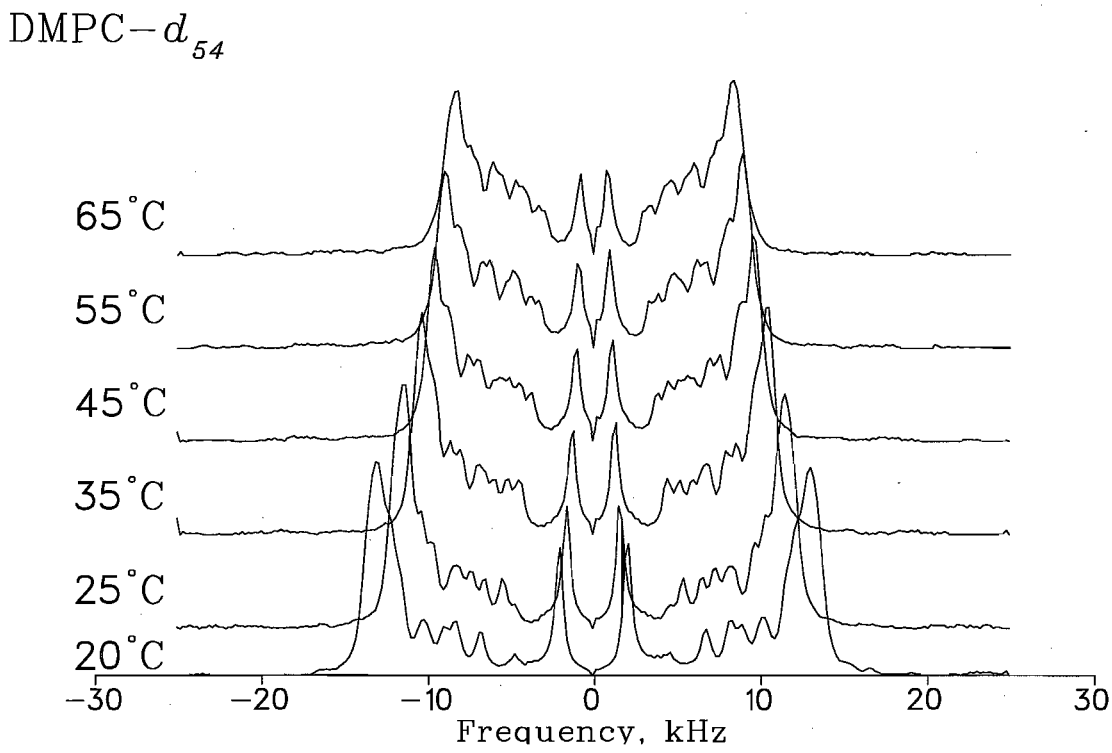

Figure 6.13: DePaked spectra of the pure DMPC sample at various temperatures.

ratio between each sample.

$$\text{signal strength} = \frac{\frac{\text{mass of lipid per sample}}{732.28\text{g/mol}} \times 54\ {}^2H \text{ atoms}}{\frac{\text{mass of drug per sample}}{549\text{g/mol}} \times 8\ {}^2H \text{ atoms}} \tag{6.1}$$

The number of scans needed for each sample was the value of the signal strength squared, because the signal-to-noise ratio is proportional to the square root of the number of scans.

The spectra of the 10:1 DMPC-d_{54}:CHX sample are illustrated in Figures 6.14 and 6.15. The spectra are again observed to narrow, indicating that motional order is decreasing with an increase in temperature. Compared with the pure DMPC spectra, there is an obvious difference in motional order. This is attributed to the presence of the small ratio of chlorhexidine in the sample. If chlorhexidine was confined to the aqueous phase, there would be no difference between the pure and 10:1 spectra.

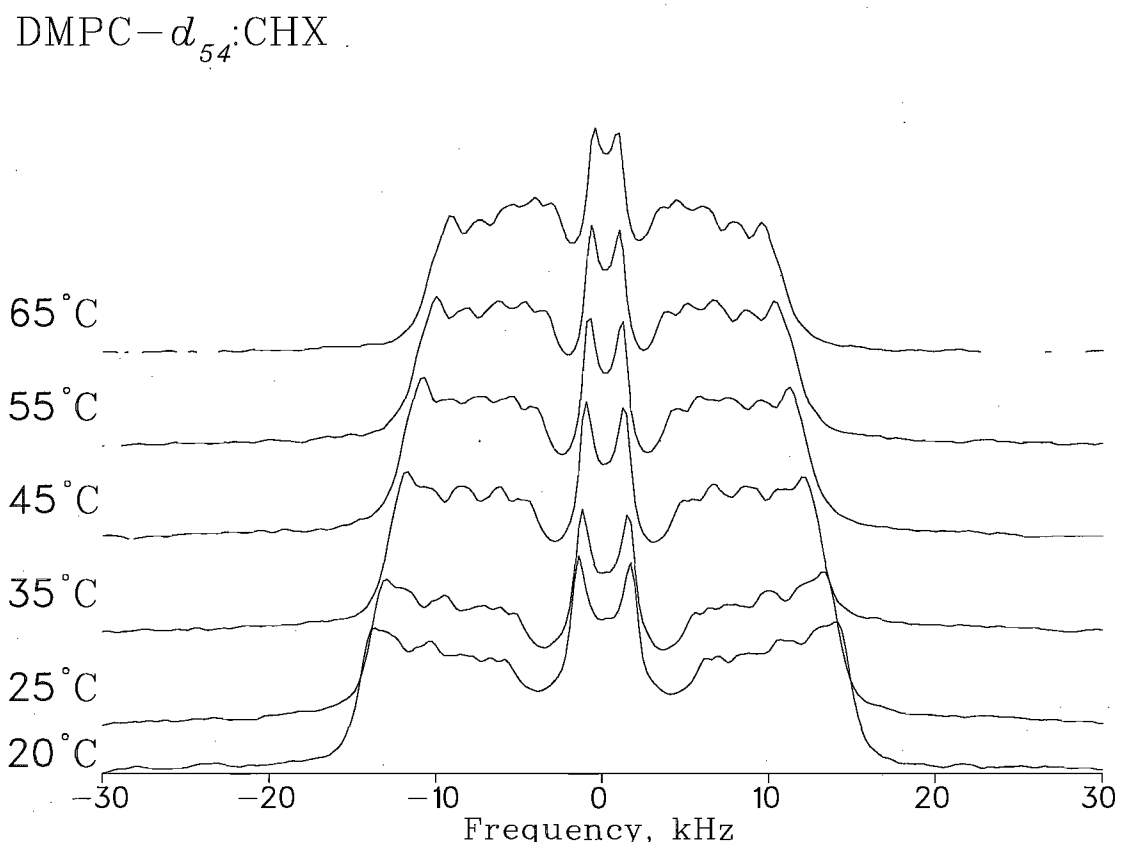

Figure 6.14: Spectra of the 10:1 DMPC-d_{54}:CHX sample at various temperatures.

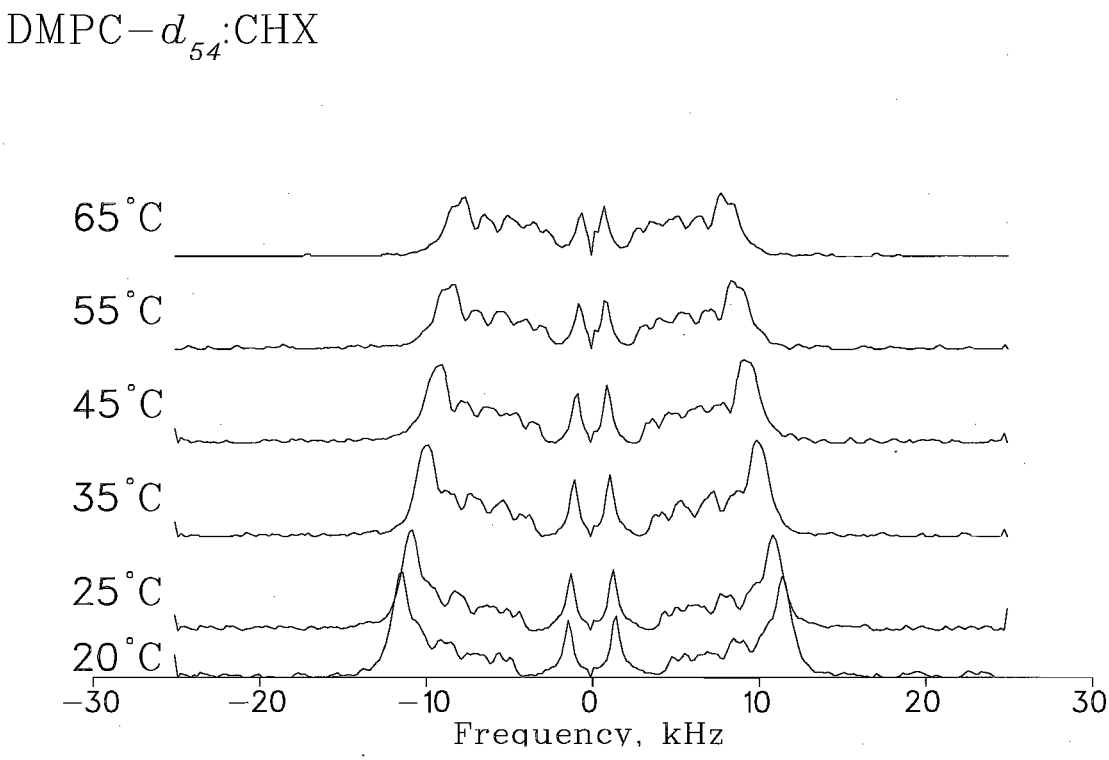

Figure 6.15: DePaked spectra of the 10:1 DMPC-d_{54}:CHX sample at various temperatures.

Figures 6.16 and 6.17 are the spectra of the 10:1 DMPC:CHX-d_8 sample. These spectra are of the motional order of the deuterium labels in the chlorhexidine molecule. Superimposing the dePaked spectra of this sample on top of the spectra of the deuterated lipid:protonated drug sample allows for a matching of the quadrupolar splittings. Recall that each peak in the spectra represents the time-average over the molecular motions. Therefore, if the peaks of the deuterated chlorhexidine are matched to peaks in the deuterated lipid, it can be expressed that those specific deuterium molecules have the same motional order. In the match-up of Figure 6.18 it is observed that the order parameter of the deuterium labels in the chlorhexdine molecule match those of the second-last and third-last CH_2 groups of the lipid. The central peak noticed in all dePaked spectra of the DMPC:CHX-d_8 samples is believed to be a residual HDO (and D_2O) peak, and was ignored for the purpose of this project.

An interesting thing to note is that not all eight deuterium atoms are resolved in the spectra. Rather, they are grouped in pairs, suggesting that the two central carbon atoms (and their respective deuterium) are moving with the same motional order, as are the second carbon atoms from the centre of the chlorhexidine molecule. This is in direct agreement of the neutron diffraction results which suggest that the chlorhexidine molecule is bent on its hexamethylene linker.

Finally, Figure 6.19 shows the dePaked spectra of the 10:1, 6:1 and 3:1 DMPC:CHX-d_8 samples. The quadrupolar splittings remain constant over the increase in drug concentration, and the order parameters also remain constant, indicating that the extent of flexing/stretching in the centre of the chlorhexidine molecule remains relatively constant, providing agreement to the hypothesis that chlorhexidine can only be in one molecular configuration when exposed to lipid bilayers.

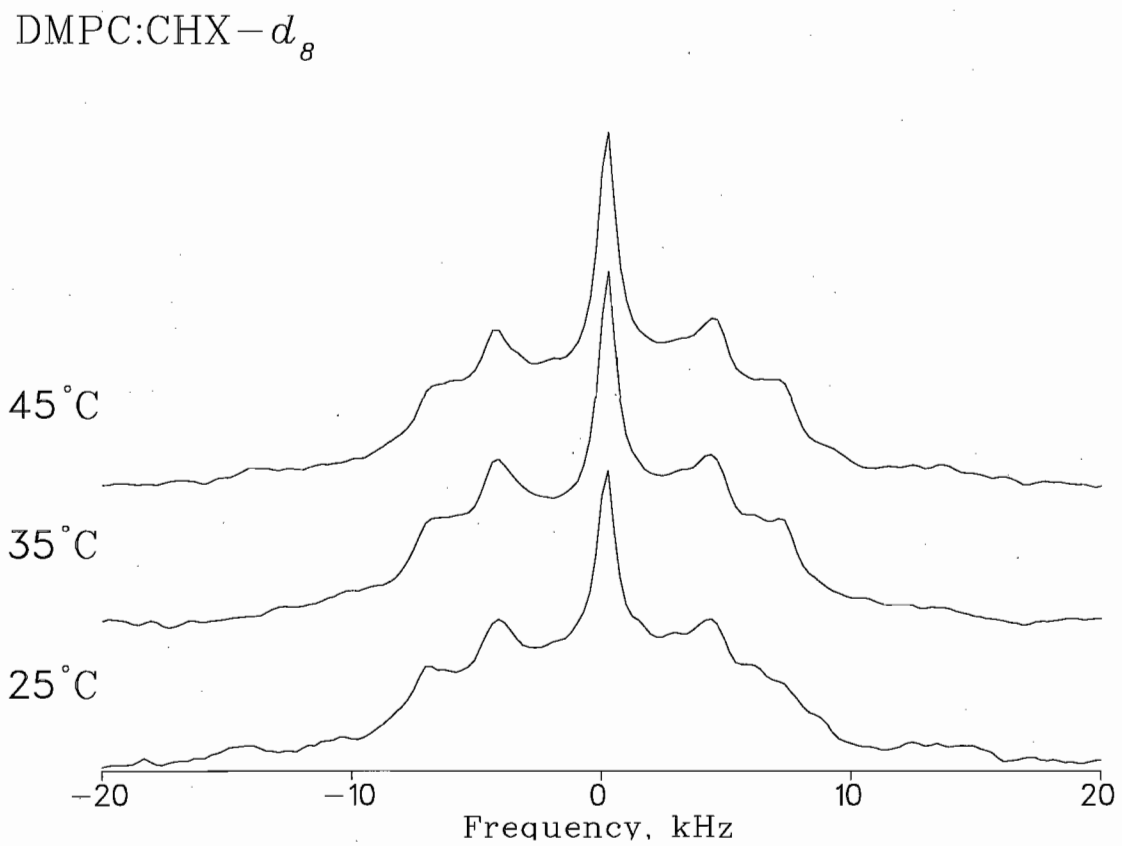

Figure 6.16: Spectra of the 10:1 DMPC:CHX-d_8 sample at various temperatures.

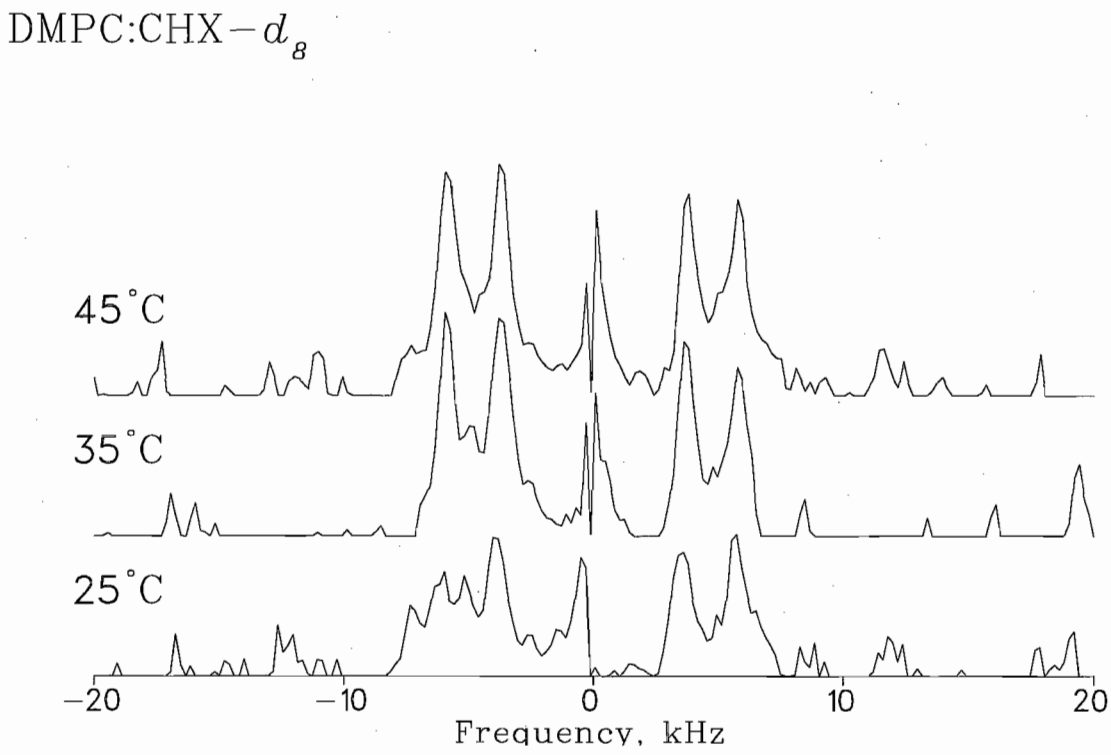

Figure 6.17: Depaked spectra of the 10:1 DMPC:CHX-d_8 sample at various temperatures.

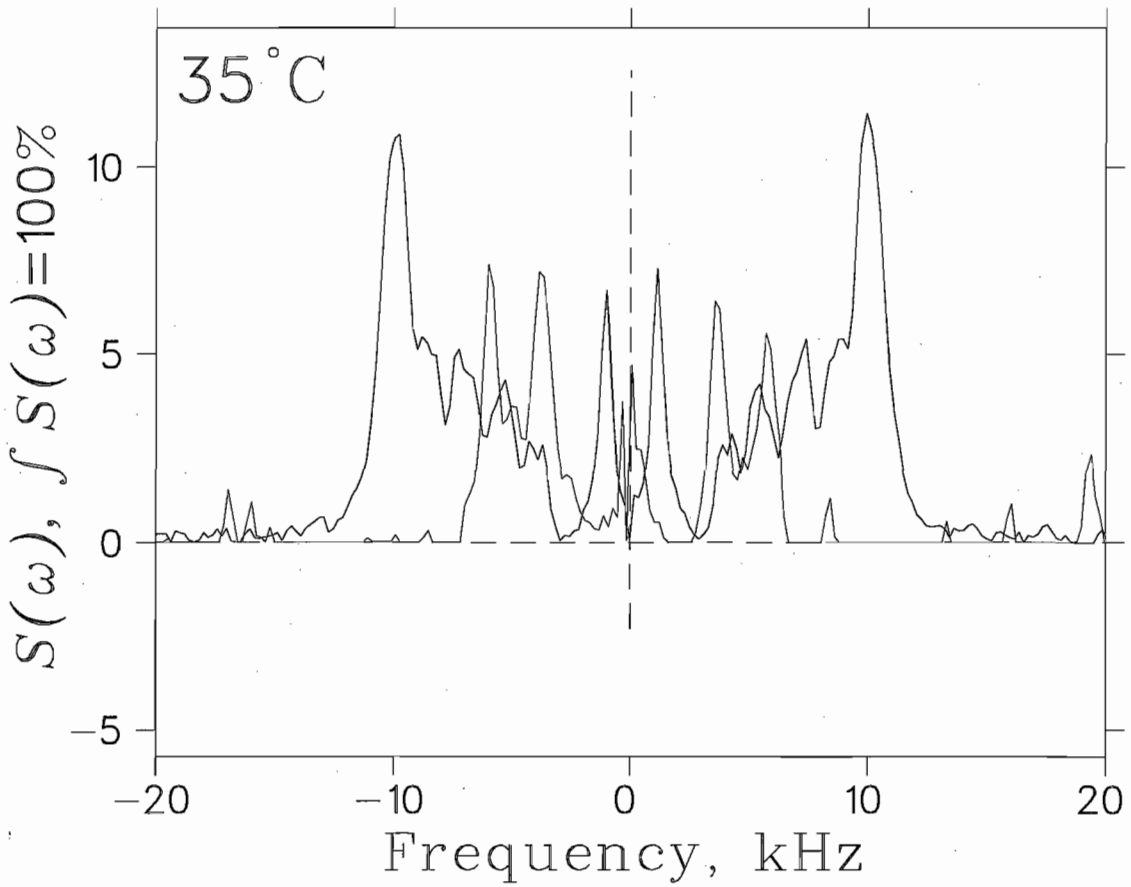

Figure 6.18: Depaked spectra of the 10:1 DMPC:CHX-d_8 sample (red line) compared with the dePaked 10:1 DMPC-d_{54}:CHX sample spectra(blue line) at 35°C.

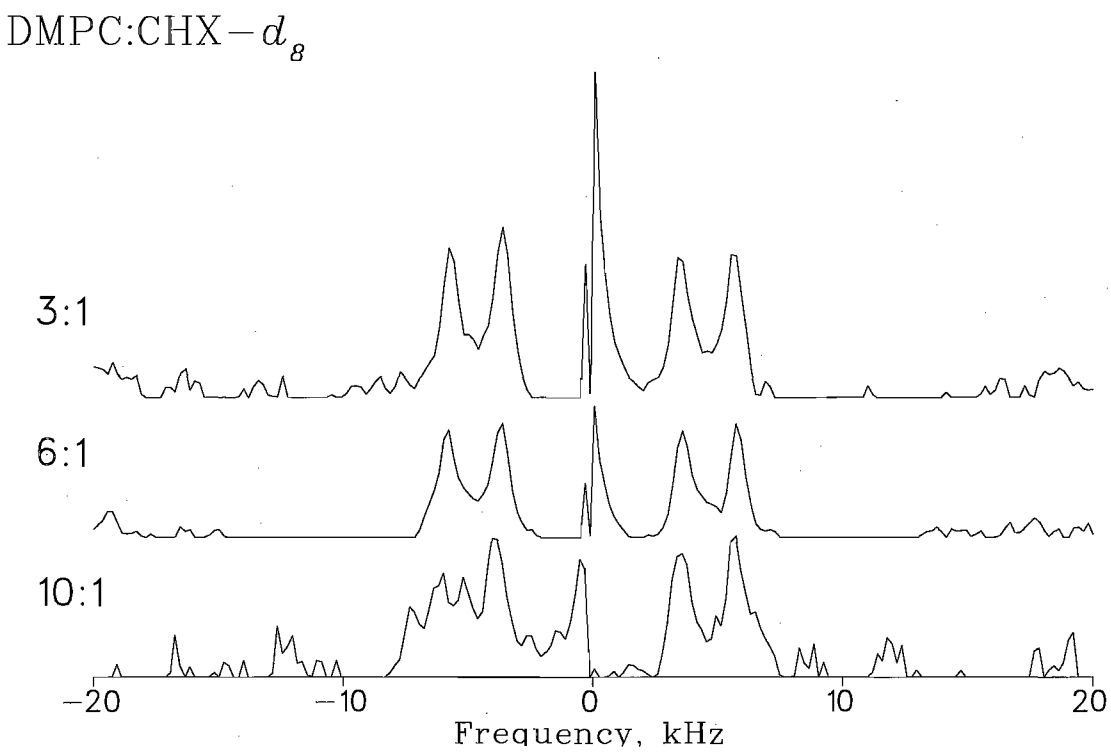

Figure 6.19: Depaked spectra of the 10:1, 6:1, and 3:1 DMPC:CHX-d_8 samples at 25°C.

Chapter 7

Conclusions

A series of biophysical experiments were conducted to describe the structural arrangement of molecules within a lipid/drug formulation.

Chlorhexidine has been established as a very powerful bactericidal agent, whose mode of action has been narrowed down to its interaction with the bacterial cell membrane [22, 23, 24, 25]. The presented data supports the hypothesis that chlorhexidine is bent double on its hexamethylene chain, thereby interacting strongly with a lipid bilayer by acting as a wedge in the lipid matrix. This provides a strong suggestion for the molecular basis of the mechanism of bactericidal action of chlorhexidine.

Early experiments on guanide, bisguanide, and bisbiguanide analogues of chlorhexidine showed that none of the individual molecular components are essential to bactericidal function [34]. A substitution of the chlorophenol by alkyl or alicyclic groups proved to be equally effective biocides. However, the bis-configuration, as well as the N^5 alkane chain length were considered important factors in biocidic function. The fact that chlorhexidine has the symmetric properties that are important to antibiotic function is in very good agreement with the proposed method of interaction.

The NMR results show the disorder of the drug remaining constant with an increase in temperature. This is not surprising. Chlorhexidine, although bent in half, is anchored at both ends by large aromatic rings, while lipids are free to move at one end, thereby showing more motional disorder as one looks down the lipid chain towards the terminal methyl group.

In the neutral, saturated lipid DMPC, chlorhexidine is bent in half on its hexamethylene, and is inserted wedge-like into the lipid bilayer. The neutron diffraction data presents the molecular picture of the hexamethylene linker residing at the juntion of the lipid headgroups and the glycerol backbones. This data rules out any biophysical model whereby chlorhexidine is stretched across the bilayer to disrupt lipid packing. This is surprising, since the hydrophobicity of the hexamethylene domain would be expected to push the drug deeper into the bilayer. Instead, an analogy of the angled insertion of antimicrobial peptides is drawn [74, 75].

Although a conclusion has been drawn, there were some limitations to this project. Only one type of lipid was studied. A cell membrane is comprised of multiple types of saturated, and poly-unsaturated lipids. This project only looked at a single saturated lipid as the model membrane system, and therefore, the partitioning of chlorhexidine in unsaturated lipids is unknown. The next step to this project is to build up the model membrane to include other types of lipids, and sterols, which act as anchors in the real membrane.

The central peak in the NMR results is taken to be a residual HDO peak. This is thought to be correct becauase the midpoint of the powder spectra and the isoropic peak do not match. However, this conclusion would be resolved with the use of high-resolution NMR techniques.

Bibliography

[1] M. Wortis and E. Evans. Membrane self-assembly: mechanical properties and vesicle shapes. *Physics in Canada*, pages 281–288, 1997.

[2] S.J. Singer and G.L. Nicolson. The fluid mosaic model of the structure of cell membranes. *Science*, 175:720–731, 1972.

[3] Clare Morrison. *Theory of the general orientation dependence of ^2H NMR spin-lattice relaxation and experiments on model membranes.* PhD thesis, University of British Columbia, 1993.

[4] D. Chapman, R.M. Williams, and B.D. Ladbrooke. Physical studies of phospholipids: thermotropic and lyotropic mesomorphism of some 1,2-diacyl-phosphatidylcholines (lecithins). *Chem. Phys. Lipids*, 1:445–475, 1967.

[5] R.B. Gennis. *Biomembranes: Molecular Structure and Function.* Springer-Verlag, 1989.

[6] A.M. Kleinfeld, P. Chu, and J. Storch. Flip-flop is slow and rate limiting for the movement of long chain anthroyloxy fatty acids across lipid vesicles. *Biochemistry*, 36:5702–5711, 1997.

[7] D.P. Tieleman, S.J. Marrink, and H.J.C. Berendsen. A computer perspective of membranes: molecular dynamics studies of lipid bilayer systems. *Biochim. Biophys. Acta.*, 1331:235–270, 1997.

[8] F. Kamp, D. Zakim, F. Zhang, N. Noy, and J.A. Hamilton. Fatty acid flip-flop in phospholipid bilayers is extremely fast. *Biochemistry*, 34:11928–11937, 1995.

[9] T.M. Allen. Liposomal drug formulations. *Drugs*, 56:747–756, 1998.

[10] M.J. Ostro and P.R. Cullis. Use of liposomes as injectable-drug delivery systems. *Am. J. Hosp. Pharm.*, 46:1576–1587, 1989.

[11] M.H. Vingerhoeds, G. Storm, and D.J.A. Crommelin. Immunoliposomes *in vivo*. *Immunomethods*, 4:259–272, 1994.

[12] E.H. Cota-Robles and D.L. Ringo. The structure of the bacterial cell. In *Microbiology*. W.B. Saunders, 1982.

[13] F.C. Neidhardt, J.L. Ingraham, and M. Schaechter. *Phisiology of the Bacterial Cell*. Sinauer Associates Inc., 1990.

[14] P. Gilbert and L.E. Moore. Cationic antiseptics: diversity of action under a common epithet. *J. Appl. Microbiol.*, 99:703–715, 2005.

[15] R.S. Blackburn, A. Harvey, L.L. Kettle, A.P. Manian, J.D. Payne, and S.J. Russell. Sorption of chlorhexidine on cellulose: mechanism of binding and molecular recognition. *J. Phys. Chem. B*, 111:8775–8784, 2007.

[16] L. Chen, L. Bromberg, T.A. Hatton, and G.C. Rutledge. Electrospun cellulose acetate fibers containing chlorhexidine as a bactericide. *Polymer*, 49:1266–1275, 2008.

[17] M.A. Al-Tannir and H.S. Goodman. A review of chlorhexidine and its use in special populations. *Special Care in Dentistry*, 14:116–122, 1994.

[18] A.D. Russell and M.J. Day. Antibacterial activity of chlorhexidine. *J. Hosp. Infect.*, 25:229–238, 1993.

[19] W.B. Hugo and A.R. Longworth. Some aspects of the mode of action of chlorhexidine. *J. Pharm. Pharmacol.*, 16:655–662, 1964.

[20] K.A. Fitzgerald, A. Davies, and A.D. Russell. Uptake of ^{14}C-chlorhexidine diacetate to *Escherichia coli* and *Pseudomonas aeruginosa* and its release by azolectin. *FEMS Microbiol. Lett.*, 60:327–332, 1989.

[21] T. El Moug, D.T. Rogers, J.R. Furr, B.M.A. El-Falaha, and A.D. Russell. Antiseptic-induced changes in the cell surface of a chlorhexidine-sensitive and a chlorhexidine-resistant strain of *Providencia stuartii. J. Antimicrob. Chemother.*, 16:685–689, 1985.

[22] S.J. Hiom, J.R. Furr, A.D. Russell, and J.R. Dickinson. Effects of chlorhexidine diacetate and cetylpyridinium chloride on whole cells and protoplasts of *Saccharomyces cerevisiae. Microbios*, 74:111–120, 1993.

[23] K. Barrett-Bee, L. Newboult, and S. Edwards. The membrane destabilizing action of the antibacterial agent chlorhexidine. *FEMS Microbiol. Lett.*, 119:249–254, 1994.

[24] T. Kuyyakanond and L.B. Quesnel. The mechanism of action of chlorhexidine. *FEMS Microbiol. Lett.*, 100:211–216, 1992.

[25] F.M. Harold, J.R. Baarda, C. Baron, and A. Abrams. DIO $_9$ and chlorhexidine: inhibitors of membrane-bound ATPase and of cation transport in *Streptococcus faecalis. Biochim. Biophys. Acta.*, 183:129–136, 1969.

[26] J.B. Park and N.-H. Park. Effect of chlorhexidine on the in vitro and in vivo herpes simplex virus infection. *Oral Surg.*, 67:149–153, 1989.

[27] M.N. Jones, Y.-H. Song, M. Kaszuba, and M.D. Reboiras. The interaction of phospholipid liposomes with bacteria and their use in the delivery of bactericides. *J. Drug Target.*, 5:25–34, 1997.

[28] J.R. Lawrence, B. Zhu, G.D.W. Swerhone, E. Topp, J. Roy, L.I. Wassenaar, T. Rema, and D.R. Korber. Community-level assessment of the effects of the broad-spectrum antimicrobial chlorhexidine on the outcome of river microbial biofilm development. *Appl. Environ. Microbiol.*, 74:3541–3550, 2008.

[29] J.J. Dynes, J.R. Lawrence, D.R. Korber, G.D.W. Swerhone, G.G. Leppard, and A.P. Hitchcock. Morphological and biochemical changes in *Pseudomonas flourescens* biofilms induced by sub-inhibitory exposure to antimicrobial agents. *Can. J. Microbiol.*, 55:163–178, 2009.

[30] J.A. Castillo, P. Clapés, M.R. Infante, J. Comas, and Á. Manresa. Comparative study of the antimicrobial activity of bis(N^{α}-caproyl-L-arginine)-1,3-propanediamine dihydrochloride and chlorhexidine dihydrochloride against *Staphylococcus aureus* and *Escherichia coli*. *J. Antimicrob. Chemother.*, 57:691–698, 2006.

[31] D.M. Deng, M.A. Hoogenkamp, J.M. Ten Cate, and W. Crielaard. Novel metabolic activity indicator in *Streptococcus mutans* biofilms. *J. Microb. Meth.*, 77:67–71, 2009.

[32] K.H. Abu-Elteen and P.A. Whittaker. Effect of sub-inhibitory concentration of chlorhexidine on lipid and sterol composition of *Candida albicans*. *Mycopathologia*, 140:69–76, 1998.

[33] T. Ikeda, S. Tazuke, and M. Watanabe. Interaction of biologically active molecules with phospholipid membranes: fluorescence depolarization studies on the effect of polymeric biocide bearing biguanide groups in the main chain. *Biochim. Biophys. Acta.*, 735:380–386, 1983.

[34] J.M. Tanzer, A.M. Slee, and B.A. Kamay. Structural requirements of guanide, biguanide, and bisbiguanide agents for antiplaque activity. *Antimicrob. Agents Chemother.*, 12:721–729, 1977.

[35] P.J. Baker, R.A. Coburn, R.J. Genco, and R.T. Evans. Structural determinants of activity of chlorhexidine and alkyl bisbiguanides against the human oral flora. *J. Dent. Res.*, 66:1099–1106, 1987.

[36] W. Zhang, E. Crocker, S. McLaughlin, and S.O. Smith. Binding of peptides with basic and aromatic residues to bilayer membranes. *J. Biol. Chem.*, 278:21459–21466, 2003.

[37] D. Stopar, R.B. Spruijt, and M.A. Hemminga. Anchoring mechanisms of membrane-associated M13 major coat protein. *Chem. Phys. Lipids*, 141:83–93, 2006.

[38] P.C.A. van der Wel, N.D. Reed, D.V. Greathouse, and R.E. Koeppe. Orientation and motion of tryptophan interfacial anchors in membrane-spanning peptides. *Biochemistry*, 46:7514–7524, 2007.

[39] M.A. Kiselev, D. Lombardo, P. Lesieur, A.M. Kisselev, S. Borbely, T.N. Simonova, and L.I. Barsukov. Membrane self assembly in mixed DMPC/NaC systems by SANS. *Chem. Phys.*, 345:173–180, 2008.

[40] D.E. Warschawski, M. Traikia, P.F. Devaux, and G. Bodenhausen. Solid-state NMR for the study of membrane systems: The use of anisotropic interactions. *Biochimie*, 80:437–450, 1998.

[41] F.A. Bovey. *Nuclear Magnetic Resonance Spectroscopy.* Academic Press, 1988.

[42] C.P. Slichter. *Principles of Magnetic Resonance.* Springer-Verlag, 1990.

[43] M.H. Levitt. *Spin Dynamics: Basics of Nuclear Magnetic Resonance.* John Wiley & Sons, 2001.

[44] J.H. Davis. The description of membrane lipid conformation, order and dynamics by ^{2}H NMR. *Biochim. Biophys. Acta.*, 737:117–171, 1983.

[45] A. Seelig and J. Seelig. Bilayers of dipalmitoyl-3-*sn*-phosphatidylcholine: conformational differences between the fatty acyl chains. *Biochim. Biophys. Acta.*, 406:1–5, 1975.

[46] H. Schäfer, B. Mädler, and E. Sternin. Determination of orientational order parameters from ^{2}H NMR spectra of magnetically partially oriented lipid bilayers. *Biophys. J.*, 74:1007–1014, 1998.

[47] H. Rust. Characterization of DMPC/DHPC mixtures by ^{31}P and ^{2}H solid-state NMR, 1998.

[48] G.E. Pake. Nuclear resonance absorption in hydrated crystals: fine structure of the proton line. *J. Chem. Phys.*, 16:327–336, 1948.

[49] M. Bloom, J.H. Davis, and A.L. MacKay. Direct determination of the oriented sample NMR spectrum from powder spectrum for systems with local axial symmetry. *Chem. Phys. Lett.*, 80:198–202, 1981.

[50] E. Sternin, M. Bloom, and A.L. MacKay. De-Pake-ing of NMR spectra. *J. Magn. Reson.*, 55:274–282, 1983.

[51] H. Schäfer and E. Sternin. Inverse ill-posed problems in experimental data analysis in physics. *Physics in Canada*, 53:77–85, 1997.

[52] H. Schäfer and R. Stannarius. Computation of orientational distributions of partially ordered samples from NMR spectra. *J. Magn. Reson. B*, 106:14–23, 1995.

[53] E. Sternin, H. Schäfer, I.V. Polozov, and K. Gawrisch. Simultaneous determination of orientational and order parameter distributions from NMR spectra of partially oriented model membranes. *J. Magn. Reson.*, 149:110–113, 2001.

[54] T.A. Harroun, G.D. Wignall, and J. Katsaras. Neutron scattering for biology. In *Neutron scattering in Biology.* Springer, 2006.

[55] G.E. Bacon. *Neutron Diffraction.* Oxford Press, 1962.

[56] M.C. Wiener and S.H. White. Fluid bilayer structure determination by the combined use of x-ray and neutron diffraction I. fluid bilayer models and the limits of resolution. *Biophys. J.*, 59:162–173, 1991.

[57] M.C. Wiener and S.H. White. Fluid bilayer structure determination by the combined use of x-ray and neutron diffraction II. composition-space refinement method. *Biophys. J.*, 59:174–185, 1991.

[58] R.N.A.H. Lewis, D.A. Mannock, and R.N. McElhaney. Differential scanning calorimetry in the study of lipid phase transitions in model and biological membranes. In A.M. Dopico, editor, *Methods in Membrane Lipids.* Humana Press, 2007.

[59] A. Blume. Biological calorimetry: membranes. *Thermochimica Acta*, 193:299–347, 1991.

[60] J.M. Sturtevant. Biochemical applications of differential scanning calorimetry. *Ann. Rev. Phys. Chem.*, 38:463–488, 1987.

[61] M. Moser, T. Hudlicky, S. Sadeghi, and E. Sternin. Synthesis of deuterium-labelled chlorhexidine. *J. Label. Compd. Radiopharm.*, 50:671–674, 2007.

[62] E. Sternin. Radio frequency phase shifting at the source simplifies NMR spectrometer design. *Rev. Sci. Instrum.*, 66:3144–3145, 1995.

[63] D.D. Heard and R.W. Ashworth. The colloidal properties of chlorhexidine and its interaction with some macromolecules. *J. Pharm. Pharmacol.*, 20:505–512, 1968.

[64] R.G. Fisher and R.P. Quintana. Surface-chemical studies on chlorhexidine and related compounds: II. interactions with monomolecular-film systems. *J. Dent. Res.*, 54:25–31, 1975.

[65] J.A. Castillo, A. Pinazo, J. Carilla, M.R. Infante, M. Ásunción Alsina, I. Haro, and P. Clapés. Interaction of antimicrobial arginine-based cationic surfactants with liposomes and lipid monolayers. *Langmuir*, 20:3379–3387, 2004.

[66] T.A. Harroun, J. Katsaras, and S.R. Wassall. Cholesterol is found to reside in the center of a polyunsaturated lipid membrane. *Biochemistry*, 47:7090–7096, 2008.

[67] D.L. Worcester and N.P. Franks. Structural analysis of hydrated egg lecithin and cholesterol bilayers II. neutron diffraction. *J. Mol. Biol.*, 100:359–378, 1976.

[68] N. Kucerka, J.F. Nagle, J.N. Sachs, S.E. Feller, J. Pencer, A. Jackson, and J. Katsaras. Lipid bilayer structure determined by the simultaneous analysis of neutron and X-ray scattering data. *Biophys. J.*, 95:2356–2367, 2008.

[69] T. Salditt. Thermal fluctuations and stability of solid-supported lipid membranes. *J. Phys. Condens. Matter*, 17:R287–R314, 2005.

[70] T.A. Harroun, M. Koslowsky, M.-P. Nieh, V.A. Raghunathan, and J. Katsaras. Finite-size effects do not reduce the repeat spacing of phospholipid multibilayer stacks on a rigid substrate. *Eur. Phys. J. E*, 13:359–362, 2004.

[71] V.I. Gordeliy and N.I. Chernov. Accuracy of determination of position and width of molecular groups in biological and lipid membranes via neutron diffraction. *Acta Crystallographica D*, 53:377–384, 1997.

[72] T. Ooi and M Oobatake. Effects of hydrated water on protein unfolding. *J. Biochem*, 103:114–120, 1988.

[73] M. Swart, T. van der Wijst, C. Fonseca Guerra, and F.M. Bickelhaupt. $\pi - \pi$ stacking tackled with density functional theory. *J. Mol. Model.*, 13:1245–1257, 2007.

[74] A. Thomas and R. Brasseur. Tilted peptides: the history. *Curr. Protein Pept. Sci.*, 7:523–527, 2006.

[75] R. Brasseur. *Moleuclar Description of Biological membranes by Comupter Aided Conformational Analysis.* CRC Press, 1990.

[76] F.-Y. Chen, M.-T. Lee, and H. W. Huang. Evidence for membrane thinning effect as the mechanism for peptide-induced pore formation. *Biophys. J.*, 84:3751–3758, 2003.

[77] B. Różycka-Roszak and A. Przyczyna. Interaction between N-dodecyl-N,N-dimethyl-N-benzylammonium halides and phosphatidylcholine bilayers–the effect of counterions. *Chem. Phys. Lipids*, 123:209–221, 2003.

[78] B. Różycka-Roszak and T. Cierpicki. ^{1}H NMR studies of micellar solutions of N-dodecyl-N,N-dimethyl-N-benzylammonium chloride. *J. Colloid Interface Sci.*, 218:529–534, 1999.

[79] S. Possidonio, F. Siviero, and O.A. Seoud. Kinetics of the pH-independent hydrolysis of 4-nitrophenyl chloroformate in aqueous micellar solutions: effect of the charge and structure of the surfactant. *J. Phys. Org. Chem.*, 12:325–332, 1999.

[80] G. D'Angelo, U. Wanderlingh, V.C. Nibali, C. Crupi, C. Corsaro, and G. Di Marco. Physical studies of dynamics in fully hydrated phospholipid bilayers. *Philosoph. Magazine*, 88:4033–4046, 2008.

[81] R. Pignatello, V.D. Intravaia, and G. Puglisi. A calorimetric evaluation of the interaction of amphiphilic prodrugs of idebenone with a biomembrane model. *J. Colloid Interface Sci.*, 299:626–635, 2006.

[82] V. Librando, M.G. Sarpietro, and F. Castelli. Role of lipophilic medium in the absorption of polycyclic aromatic compounds by biomembranes. *Environ. Toxicol. Pharamcol.*, 14:23–32, 2003.

[83] M. Szögyi, T. Cserháti, and L. Lelkes. Differential scanning calorimetry to study the possible ternary complex formation between chlorhexidine, phosphatidylcholine and some nonionic tenzides. *J. Biochem. Biophys. Methods*, 23:31–43, 1991.